Deep Blue Retrievals of Asian Aerosol Properties During ACE-Asia

N. Christina Hsu, Si-Chee Tsay, Michael D. King, *Senior Member, IEEE*, and

Jay R. Herman

IEEE Transactions on Geoscience and Remote Sensing

N. C. Hsu, S. C. Tsay, M. D. King, and J. R. Herman are with the Earth-Sun Exploration Division, NASA Goddard Space Flight Center, Greenbelt, MD 20771 USA (e-mail: hsu@climate.gsfc.nasa.gov).

Abstract—During the ACE-Asia field campaign, unprecedented amounts of aerosol property data in East Asia during springtime were collected from an array of aircraft, shipboard, and surface instruments. However, most of the observations were obtained in areas downwind of the source regions. In this paper, we employ the newly developed satellite aerosol algorithm called "Deep Blue" to characterize the properties of aerosols over source regions using radiance measurements from SeaWiFS and MODIS. Based upon the Angstrom exponent derived from the Deep Blue algorithm, we demonstrate that this new algorithm is able to distinguish the dust plumes from fine-mode pollution particles, even in complex aerosol environments such as the one over Beijing. Furthermore, we validate these results by comparing them to the observations from AERONET sites in China and Mongolia during spring 2001. These comparisons show that the values of satellite retrieved aerosol optical thickness from Deep Blue are generally within 20 % to 30% of those measured by sunphotometers.

Our analyses also indicate that the roles of mineral dust and anthropogenic particles are comparable in contributing to the overall aerosol distributions during spring in northern China, while fine mode particles are dominant over southern China. The spring season in East Asia consists of one of the most complex environments in terms of frequent cloudiness and wide ranges of aerosol loadings and types. We will discuss how the factors contributing to this complexity influence the resulting aerosol monthly averages from various satellite sensors and, thus, the synergy among satellite aerosol products.

I. INTRODUCTION

The impact of growing air pollution in Asia, and other parts of the world, has gained increasing attention from the scientific community in recent years. Among the many components that contribute to such pollution, airborne mineral dust plays an important role due to its biogeochemical impact on the ecosystem and its radiative-forcing effect on the climate system [8], [13]. In East Asia, dust storms frequently accompany the cold and dry air masses that occur as part of springtime cold front systems. China's capital, Beijing, and other large cities are on the primary pathway of these dust storm plumes, and their passage over such population centers causes flight delays, pushes grit through windows and doors, and forces people indoors. Furthermore, during the spring these anthropogenic and natural air pollutants, once generated over the source regions, can be transported out of the boundary layer into the free troposphere and can travel thousands of kilometers across the Pacific into the United States and beyond. Satellite views, as shown in Fig. 1, illustrate the vast distances over which these Asian dust plumes can extend. Once caught by the westerly jet, these pollutant clouds have been shown to reach as far as North America [28] and the French Alps [7].

Because of their complexity, it is especially important to understand the processes controlling the formation, transport, and fate of aerosol types occurring from East Asian source regions into areas downstream. Properties of Asian dust and anthropogenic pollution aerosols have been extensively studied using information collected during the ACE-Asia field campaign [15]. Yet most of the observations during the experiment were obtained in areas downwind of the source region. This is due to the fact that retrieving aerosol properties over dust source regions (i.e., arid and semi-arid regions) using the traditional Advanced Very High Resolution Radiometer (AVHRR) channels in the visible and near IR wavelengths is a difficult task because of the bright underlying surfaces over such regions [18]. There have been several approaches developed to retrieve aerosol opti-

1

cal properties over the desert, including contrast reduction (atmospheric blurring) and thermal property techniques [26], [27]. However, since contrast reduction using visible wavelengths depends on the selection of highly contrasted areas as retrieval targets, this approach might not be straightforward for most desert regions. For thermal techniques, the separation of the signal due to mineral aerosols from that due to the background temperature and water vapor signals of the terrestrial environment can be complicated and unreliable, particularly over semi-arid regions. The latter (i.e., thermal approach) in particular presents a difficult problem for retrieving aerosol properties in East Asia, since the amounts of atmospheric water vapor, aerosol plume height, and surface temperature and emissivity are highly variable and not well known during the spring.

In this study, we present results on retrieved aerosol properties over source regions in East Asia by employing a newly developed aerosol algorithm called "Deep Blue" on satellite radiance measurements taken from SeaWiFS and MODIS. The detailed description of the Deep Blue algorithm and its application to derive aerosol properties over the Sahara Desert were previously discussed in Hsu *et al.* [14]. In Section 2 of this paper, we first discuss results of theoretical simulations performed to examine the advantages and disadvantages of retrieving aerosol properties using different satellite channels from the UV to visible part of spectrum. A brief overview of the Deep Blue algorithm and the derived spectral characteristics of surface reflectance for deserts in East Asia are then given in Section 3. The Level 2 daily maps of aerosol properties determined from Deep Blue and the use of aerosol optical thickness measurements obtained from several AERONET sites during ACE-Asia to validate the Deep Blue aerosol products are discussed in Sections 4 and 5, respectively. The resulting monthly averaged maps of retrieved aerosol optical thickness and Ångström exponent, which present the overall distributions of dust and anthropogenic pollution aerosols over source regions during March and April 2001, are shown in Section 6. Finally, we discuss the synergy of aerosol information using

multi-platform sensors from SeaWiFS, MODIS, and the Multiangle Imaging SpectroRa-diometer (MISR) in Section 7, followed by the conclusion in Section 8.

II. Optimal Method of Aerosol Retrievals over Arid and Semi-Arid Areas

In order to explore the optimal methods of retrieving aerosol properties from UV to visible wavelengths over arid and semi-arid regions using satellite reflectance measurements, we employ a thoroughly tested radiative transfer model [4] to compute the reflected intensity field, which is defined by

$$R(\mu,\mu_0,\phi) = \frac{\pi I(\mu,\mu_0,\phi)}{\mu_0 F_0},$$

where R is the normalized radiance (or apparent reflectance), F_0 is the extra-terrestrial solar flux, I is the radiance at the top of the atmosphere, μ is the cosine of the view zenith angle, μ_0 is the cosine of the solar zenith angle, and ϕ is the relative azimuth angle between the direction of propagation of scattered radiation and the incident solar direction.

This radiative transfer code includes full multiple scattering and takes into account polarization. Within the blue wavelength range (e.g., 412 to 490 nm), where Rayleigh scattering is relatively important compared to the longer wavelengths, neglect of polarization in the radiative transfer code leads to significant errors in the calculated reflectances [25]. To simulate the apparent reflectances received by satellite sensors, we use the spectral surface reflectance information from 340 nm to 670 nm as depicted in Fig. 2a (line with asterisks). These values are representative of surface properties over deserts based upon the Total Ozone Mapping Spectrometer (TOMS) and SeaWiFS databases described in Section 3B. For aerosol properties, we select two types of dust aerosols for the simulations. One represents moderately absorbing pure dust (D2), while another resembles dust coated by a slight amount of soot (D1). The corresponding values of single scattering albedo (ω_0) over this spectral domain for each type, ranges from 0.92 to 1.0 for D2 (line with closed circles) and from 0.89 to 0.987 for D1 (line with open circles), are shown in

Fig. 2a. The Ångström exponent (α) was set to zero for the spectral shape of aerosol optical thickness, and the vertical profile of the aerosol layer was assumed to be Gaussian with a peak at 3 km and a width of 1 km. The values of aerosol optical thickness (τ_a) are set to unity.

To account for the effect of nonspherical dust particle shapes, an "effective phase function" was used in the dust models instead of one calculated by assuming Mie scattering for particle sizes representative of dust aerosols. This "effective phase function" was previously derived empirically to give the best fit of the satellite-retrieved τ_a using our SeaWiFS aerosol algorithm over ocean to the measured τ_a by the ground-based AERONET sunphotometer site at Cape Verde (*cf.* Fig. 7 in Hsu *et al.* [14]).

A solar zenith angle $\theta_0 = 20^o$, relative azimuth angle $\phi = 120^o$, and view zenith angles $\theta = 0^o$, 40°, and 60° are chosen to perform the simulations. These viewing geometries are typical for SeaWiFS and MODIS. To examine the sensitivity for detecting the presence of aerosols over deserts from the UV to visible wavelengths, we define an "Efficiency Index" parameter as

$$EI = Efficiency \ Index = 100 * \frac{R_{aero} - R_{Ray}}{R_{Ray}},$$

where R_{aero} represents the reflectance in the presence of aerosols and R_{Ray} is the reflectance for a Rayleigh scattering atmosphere only. The Efficiency Index, *EI*, is equivalent to the percent change in the apparent reflectance at a given channel in going from a Rayleigh only (aerosol-free) atmosphere to a Rayleigh atmosphere containing aerosols.

As shown in Fig. 2b, *EI* peaks at 412 nm for both aerosol types for a nadir looking geometry. This is a result of two competing factors. The brighter surface diminishes the contrast between the aerosol backscatter and the surface reflectance (i.e., *EI* decreases) at longer wavelengths, while strong dust absorption tends to lessen the excess reflectance introduced by the presence of dust aerosols at shorter wavelengths. At $\theta = 60^o$, *EI* is

comparable at both 412 and 490 nm. This is due to the fact that when the sensor's view zenith angle is larger, the slant path is longer and the surface effect on the apparent reflectance is reduced compared to the nadir view. This results in a more dominant role for aerosol absorption in defining the spectral shape of the apparent reflectance that leads, in turn, to more comparable aerosol signals at 412 and 490 nm.

Next, we investigate the sensitivity of apparent reflectance from the UV to visible wavelengths to aerosol height as well as the resulting errors in retrieved τ_a and ω_0. Since the plume heights of tropospheric aerosols are uncertain, but are usually between 1 and 5 km, theoretical simulations were performed assuming different aerosol vertical profiles using Gaussian distributions with a width of 1 km centered at 1, 3, and 5 km. The nadir view results for the D2 model are displayed in Fig. 3. The values of solar zenith angle and relative azimuth angle used in these calculations are the same as in Fig. 2b. As shown in Fig. 3a, the calculated apparent reflectance with different aerosol altitudes deviates from one another significantly at 340 nm and becomes almost indistinguishable at 490 and 670 nm. Although not shown here, a similar pattern also applies to results using the D1 model. The corresponding errors in retrieved τ_a from 340 to 670 nm for the D2 model are depicted in Fig. 3c where the assumed retrieval height is 3 km, while the actual plume heights were 1 and 5 km. While the uncertainty in estimated τ_a due to variation in aerosol altitude is roughly 10-15% at 412 nm, it reaches up to 75% at 340 nm. An even larger uncertainty at 340 nm for the D1 model is observed. Thus, reduced plume-height sensitivity for the deep blue to visible wavelengths is an advantage for analyzing SeaWiFS and MODIS data.

Errors in the retrieved ω_0 for different wavelengths introduced by aerosol altitude uncertainty were also examined. The results, shown in Fig. 3b, indicate that the calculated apparent reflectance for the same aerosol plume at different aerosol heights of 1, 3, and 5 km becomes further separated as the wavelength gets shorter. At 340 nm, the aero-

sol layer appears darker at 5 km and brighter at 1 km when compared to its appearance at 3 km. The reflectance at 670 nm, on the other side, does not change as a function of aerosol vertical profile. As a result, if the actual ω_0 was 0.94, the retrieved value of ω_0 could be underestimated or overestimated by approximately 0.02 at 340 nm, approximately 0.01 at 412 nm, and only 0.004 at 490 nm (see Fig. 3d). For a view zenith angle of 40°, the magnitudes of these errors are similar to those of the nadir view.

There are many methodologies for retrieving atmospheric aerosols under various environmental conditions, as one can find in the published literature [18]. However, considering the two competing factors of efficiency and error depicted in Figs. 2 and 3, it is clear that the Deep Blue algorithm is the optimal method for retrieving aerosols over high reflectance arid and semi-arid areas. To further demonstrate the broad applications of Deep Blue over other regions of the Earth is outside the scope of this paper.

III. SATELLITE DATA AND METHODOLOGY

The aerosol information presented in this study is derived from the Deep Blue algorithm, which can be applied to measurements taken from SeaWiFS and MODIS-like sensors. The Deep Blue algorithm employs a different approach from the current MODIS aerosol retrieval algorithm over land, which uses the dark-target approach [16], [17] and assumes the ratio of surface reflectance between 0.47 μm (0.64 μm) and 2.1 μm is 0.25 (0.5). This assumption is valid for most vegetated land surfaces [3]. However, over desert regions, land surface reflectance significantly deviates from this assumption. As a result, there are substantial areas with data gaps in retrieved aerosol properties over land using the current MODIS algorithm.

The Deep Blue algorithm alleviates such problems in detecting aerosol properties over brightly reflecting surfaces by employing radiances from the blue channels of these instruments, where the reflectance is low enough to make such retrievals possible. In this section, we will briefly review the fundamental elements of the Deep Blue algorithm. De-

tails of the Deep Blue satellite retrieval algorithm are described further in Hsu *et al.* [14].

A. Description of Deep Blue Algorithm

To provide a quick look at the structure of the algorithm, a schematic flow chart is shown in Fig. 4. The first step in our satellite-processing stream is to apply a Rayleigh correction for terrain elevation to the measured reflectances to account for variations in the surface pressure (for details see Section 3C). Then, before the aerosol retrieval processing begins, we screen out scenes for the presence of sub-pixel clouds by examining both the spatial homogeneity within 3 pixels by 3 pixels and absorbing aerosol index values. Currently, aerosol retrievals over cloud-contaminated scenes have not been furnished due to its complexity. The surface reflectance for a given pixel is determined from a clear-scene database based upon its geolocation. The reflectances measured at 412, 490, and 670 nm channels (from SeaWiFS) or those at 412, 470, and 650 nm channels (from MODIS) are then compared to radiances contained in a look-up table with dimensions consisting of solar zenith, satellite zenith, and relative azimuth angles, surface reflectance, aerosol optical thickness, and single scattering albedo. A maximum likelihood method is used to compute a mixing ratio between various dust models and smoke models until the calculated spectral reflectances make the best match to those that are measured. We also employ iterative procedures to obtain optimal information for various aerosol and surface conditions [14]. For mixed aerosol conditions, once the aerosol models and the mixing ratio that produce the best match are determined, the values of aerosol optical thickness and Ångström exponent are reported. For dust dominant cases, the values of single scattering albedo are retrieved (c.f. Fig. 8 in Hsu et. al. [14]) in addition to aerosol optical thickness and Ångström exponent.

B. Surface Reflectances over Asian Deserts

As described in Hsu *et al.* [14], the Deep Blue algorithm uses a pre-calculated sur-

face reflectance database developed by employing the minimum reflectivity technique to determine the surface boundary condition. Compared to vegetated land surfaces, deserts and semi-deserts have a weak surface bidirectional reflectance distribution function (BRDF) effect, particularly for blue wavelengths. However, when the aerosol loading is small, the neglect of surface BRDF effects could still potentially lead to a significant error in the retrieved τ_a value. In order to improve upon the Lambertian surface reflectance assumption used in Hsu *et al.* [14], we construct a surface reflectance database by binning the reflectance according to viewing geometry, and we subsequently determine the minimum reflectivity for the corresponding bin. Our results indicate that, for the mid-latitude deserts and semi-deserts in East Asia, the effect of surface BRDF over the blue wavelengths is negligible on the retrieved τ_a value for larger solar zenith angle ($>40^0$) during March and April but needs to be taken into account when the solar zenith angle is smaller than 40^0. This is consistent with the surface observation findings made over the Gobi desert using the ASD spectroradiometer [21].

Fig. 5a and 5c show the resulting East Asia land surface reflectance database calculated at 412 nm (from SeaWiFS) and 650 nm (from MODIS) for spring 2001 (March, April, and May). The resolution of this database is 0.1° in latitude by 0.1° in longitude. It is apparent that the surface reflectance is brighter in northern and western China as well as in the vicinity of southern Mongolia and western Kazakhstan compared to the rest of East Asia; these areas are associated with a series of arid and semi-arid areas in a 40° to 50° N latitude zone. Within this desert zone, the values of surface reflectance are generally smaller than 0.08 at 412 nm and 0.3 at 650 nm, except for a few limited extreme bright areas near the northern and eastern borders of the Taklimakan desert. These brighter surfaces over the Taklimakan desert are the results of mixtures of desert sands and areal patches of hard-shell salt compounds that formed by the dryness of seasonal ground water from the surrounded high mountain ranges. According to the Deep Blue

surface database, the spectral dependence of the surface reflectance over the Taklimakan desert also appears to be much flatter than that of the Gobi desert in southern Mongolia. The ratio between the surface reflectance at 412 nm and 670 nm is approximately 1 : 2 vs. 1 : 4 for the Taklimakan and Gobi Deserts, respectively. This may be related to the inherent differences in dust composition and grain sizes between these two different sources.

To compare values of surface reflectance at the 412 nm channel from SeaWiFS with the 380 nm channel from TOMS, we also display the minimum reflectivity database calculated using 16 years of TOMS measurements for the spring season (March, April, and May) [10]. This dataset is gridded at 1° latitude by 1.25^o longitude because of the coarse spatial resolution of the TOMS instrument (100 km average and 50 km at nadir). As shown in Figs. 5a and 5b, the values of surface reflectance at 412 nm are generally close to those at 380 nm. However, due to different spatial resolutions between these two datasets, a number of fine geographic features, such as the edges of the Taklimakan desert, appear to be smoothed out in the TOMS dataset. There are also fewer gaps in the TOMS data set because it is composed of 16 years of observations and thus is able to obtain more pixels taken under snow/ice free conditions.

Most of the deserts shown in Fig. 5c are aged and naturally made as a result of the low annul rainfalls mentioned above. In order to examine the potential effects of human activities on the distributions of dust sources, we also include the map of dust erodible fraction estimated from the USGS land cover data depicted in Fig. 5d. This dataset is based upon the land conditions observed during the early 1990s. A significant area in the eastern part of Inner Mongolia just northwest of Beijing (42° to 47° N, 110° to 124° E) is identified in Fig. 5c as arid and semi-arid regions. However, this area is not shown in the USGS land cover dataset shown in Fig. 5d. This suggests that more desert and semi-desert regions have formed between the early 1990s and 2001, possibly caused by an-

thropogenic activities such as overgrazing and overplowing. Similar conclusions were also obtained by Liu *et al.* [20] using Landsat TM imagery, indicating that there was a substantial land transformation in this part of China during the period 1990 to 2000. Indeed, these new dust sources are believed to have caused many of the dust storm events that were not correctly identified during the ACE-Asia campaign by dust model forecasts that assumed locations for dust sources similar to those in the USGS map [2], [29].

C. Rayleigh Correction for Elevation Effect

To account for the pressure dependence of Rayleigh scattering associated with surface elevation, we generated two lookup tables: one for a surface pressure of 1 atmosphere and the other for a surface pressure of 0.4 atmospheres. The ETOPO5 global 5-minute gridded elevation dataset archived at NOAA's National Geophysical Data Center (NGDC) (URL: http://www.ngdc.noaa.gov/mgg/fliers/93mgg01.html) is used in our algorithm to interpolate between the two pressure tables. A correction in reflectance is then applied to each satellite pixel using the difference in Rayleigh scattering calculated between the surface pressure at the actual geographical elevation and sea level for the observed viewing geometry.

Although the Rayleigh correction is small for the 670 nm wavelength, neglect of such effects could lead to substantial errors for the 412 nm channel over high terrain regions. For example, a nadir looking measurement of a scene with a surface reflectance of 0.04, τ_a value of 0.1, surface pressure of 850 hPa, solar zenith angle of 20°, and relative azimuth angle of 120°, would retrieve values of surface reflectance and τ_a of 0.012 and 0.15, respectively, at 412 nm assuming a surface pressure of 1 atmosphere. Therefore, the surface reflectance could be underestimated by 0.028 and τ_a overestimated by as much as 50% at 412 nm if the effect of elevation is neglected.

IV. RETRIEVING AEROSOL PROPERTIES DURING ACE-ASIA

In order to investigate the evolution of aerosols in this region, we applied the Deep Blue algorithm described above to both SeaWiFS and MODIS. Daily maps of aerosol properties in the cloud free regions over East Asia have been generated with a 1 x 1 km spatial resolution. Fig. 6 shows an example of dust events observed by SeaWiFS in East Asia during April 6-7, 2001. As mentioned previously, this time period coincides with the ACE-Asia field campaign that took place from March through May of that year. The satellite retrieved values of τ_a, α, and ω_0 for each day are depicted in the panels from top to bottom, respectively. The combination of τ_a and α provides information on the column-averaged characteristics of the air mass that can be used to distinguish dust from anthropogenic pollution aerosols. For example, Fig. 6a indicates that, on April 6, 2001, dust clouds were observed over the Taklimakan desert as well as over the Gobi desert and the deserts of central Inner Mongolia, while eastern China and Southeast Asia were dominated by fine-mode anthropogenic pollution (smoke) as indicated by the Ångström exponent values shown in Fig. 6c. This dust storm was triggered by a strong low-pressure system that developed over eastern Mongolia, producing heavy dust plumes over the Gobi desert and regions south of the Gobi. This system continued to strengthen as it moved eastward to Inner Mongolia on April 7, creating an enormous dust cloud covering a vast area as depicted in Fig. 6b. A north-south gradient in Ångström exponent over eastern China was particularly distinct on this day as the airmass transitioned from one dominated by dust in the north (small Ångström exponent) into one dominated by fine mode air pollution in the south (large Ångström exponent) as shown in Fig. 6d.

There are also significant differences in aerosol absorption values retrieved by the Deep Blue algorithm over different dust plumes. As displayed in Fig. 6e, the northern dust plumes observed on April 6 over the Gobi in Mongolia appeared to be more absorbing ($\omega_0 \sim 0.87$) at 412 nm than the southern ones located over central Inner Mongolia and

the Taklimakan ($\omega_0 \sim 0.94\text{-}0.95$). To contrast the colors between these two dust plumes, the spectral apparent reflectances measured by SeaWiFS from 412 to 865 nm over the Mongolian dust plume are compared in Fig. 7 to those measured over the Inner Mongolian plume. The reflectances observed at these locations during a clear day, when dust was low, are also included in the figure. It is apparent that the surface properties at these two locations are similar by looking at the clear day cases. However, the spectral signatures are dramatically different between the two dusty cases throughout the entire spectral range from the visible to the near IR. In fact, the Mongolia dust plume is so absorbing in the shorter wavelengths that the plume itself became invisible to Earth Probe TOMS, which measured collocated reflectances on the same day at 340 and 380 nm.

Based upon the error analyses shown in Fig. 3, such a difference in ω_0 cannot be caused by a difference in altitude between these two dust plumes. In fact, several aerosol transport modeling results indicate that the peaks of the dust plumes over southern Mongolia are not higher than those over central Inner Mongolia in China on April 6 [22]. This difference in spectral characteristics of the two plumes may well be the indicator of different dust compositions related to their source regions, as discussed in section 3B.

V. VALIDATION

Five AERONET sites [11] were operating in China and Mongolia during the 2001 ACE-Asia period: Dunhuang, Yulin, Inner Mongolia, Beijing, and Dalanzadgad. In Fig. 8, the locations of these sites are superimposed on the terrain elevation values from the ETOPO5 5-minute gridded database that is used in our satellite algorithm. Detailed characteristics of the data from these five AERONET sites are displayed in Table 1. Except for Beijing, all these AERONET sites are at elevations higher than 1 km, particularly the site at Dalanzadgad ($\sim$ 1.5 km). Fig. 9 depicts the relationship between aerosol optical thickness and Ångström exponent collected during April 2001 by the ground-based sunphotometers at Dunhuang, Inner Mongolia, and Dalanzadgad, respectively. While the

minimum τ_a values were 0.09 and 0.05 for Inner Mongolia and Dalanzadgad, respectively, the value of τ_a was never observed to be lower than 0.18 at Dunhuang for this month. However, sunphotometer data from May 2001 (not shown here), when the airborne dust level decreased at Dunhuang, showed values lower than 0.18, and the values of Ångström exponent varied as a function of τ_a in a similar fashion as those of both Dunhuang and Dalanzadgad. The data shown in Fig. 9 indicate fine mode particles as background aerosols for these three sites. However, the air mass over Dunhuang and Dalanzadgad was mostly dominated by mineral dust in April 2001, while Inner Mongolia was under the influence of both dust and fine mode pollution.

Comparisons between τ_a retrieved from SeaWiFS level 2 data using the Deep Blue algorithm and the AERONET sites at Dunhuang, Yulin, Inner Mongolia, and Dalanzadgad during ACE-Asia (March-May, 2001) are shown in Fig. 10. These collocated data were compiled using criteria that the satellite pixels must be within 10 km from the AERONET sites and taken within a window of 15 minutes between the satellite overpass and the sunphotometer observation time. Due to the frequent occurrence of clouds in this region during springtime, there is only a limited number of cloud-free satellite retrievals collocated with the AERONET sunphotometer data. The comparisons indicate that the agreement between satellite-retrieved τ_a and sunphotometer values are generally within 30% of the sunphotometer τ_a measurements for all four sites.

Compared to the three sites in Fig. 9, Beijing is in a much more complex environment in terms of aerosol properties. In the spring, Beijing is on the primary path of both fine-mode pollution and transported dust clouds. As depicted in Fig. 11a, most Ångström exponent values range between 0.5 and 1.3, with no obvious pattern in the aerosol optical thickness−Ångström exponent relationship. This indicates that both fine mode and coarse mode particles are equally dominant in the air mass over Beijing during this season. Even with such a complex environment, aerosol properties retrieved from the Deep Blue algo-

rithm compared reasonably well with those from AERONET ground-based sunphotome-
ter measurements, as depicted in Fig. 11b and 11c. The Deep Blue algorithm is able to
successfully separate the fine mode contribution from the coarse mode contribution, and
the resulting values of τ_a at 490 nm retrieved from SeaWiFS are generally within 20% of
those at 500 nm from AERONET.

VI. MONTHLY STATISTICS OF AEROSOL PROPERTIES IN THE SPRING SEASON

To study the overall aerosol distribution patterns in East Asia, we also compute
monthly means of aerosol properties for a 1° x 1° grid placed over the region. Due to fre-
quent cloud cover in this region during springtime, we use criteria that require a mini-
mum sample number of 6 cloud-free days in order to calculate the monthly mean for each
grid box. Fig. 12 depicts the monthly averaged values of aerosol optical thickness and
Ångström exponent in East Asia derived from the SeaWiFS Deep Blue algorithm for
March and April 2001. During March 2001, Fig 12a shows that elevated aerosol loading
levels were observed around the East China Sea, the Yellow Sea, eastern China, and the
Korean peninsula. This elevated aerosol loading is partly attributed to the long-range
transport of dust, but also contains a contribution from fine mode pollution in the eastern
part of China. As seen in Fig. 12c, these fine mode pollution aerosols also contribute to
high values of τ_a seen over the Sichuan basin and over the heavy industrial regions along
the Yangtze River. However, because the pathways for dust go through the urban and in-
dustrial regions in the northern part of China, the monthly mean values of Ångström ex-
ponent are significantly lower in the north compared to those in the southern part of
China. Similar spatial distributions of thick haze generated by anthropogenic activities
reoccurred in April 2001, as seen in Figs. 12b and 12d.

For the northwest part of China, elevated values of aerosol loading were also ob-
served in March 2001 as a result of dust storms generated from sources over the Takli-
makan desert and deserts in Inner Mongolia. Based upon our satellite analysis using Deep

Blue SeaWiFS and MODIS aerosol products, both the intensity and frequency of these dust storms increased in April 2001 over East Asia compared to March 2001. As observed in the satellite images, all the dust sources in the Gobi desert, the Taklimakan desert, and Inner Mongolia were quite active, and they continuously pumped dust into the atmosphere during this period. A number of these dust plumes were picked up by the jet stream and were subsequently observed to travel across the Pacific, resulting in elevated aerosol loading seen at higher latitudes over ocean in Fig. 12b.

These monthly maps of Ångström exponent values also reveal the primary dust transport pathways in the region, which are largely influenced by the effect of topography depicted in Fig. 8. The natural funneling of large air masses by the high mountains in northwestern China, combined with the high plateaus in Mongolia, helps to channel dust plumes lifted from the Taklimakan desert, the Gobi area and Inner Mongolia into the eastern and northeastern part of China and, subsequently, over the Korean Peninsula and Japan. This combination creates a primary dust pathway along the 35° to 45° N latitude bands in the region. However, besides the east- and northeastward transport pattern, dust clouds can also be brought into the southern part of China, influencing the visibility and air quality in this region [29]. This southbound dust route is clearly visible in the April 2001 Ångström exponent map depicted in Fig. 12d.

During the ACE-Asia experiment period, there was also extensive biomass burning activities over Southeast Asia, as well as over Siberia along the Amur River near the China/Russia border. These biomass-burning fires raised the proportion of fine mode smoke aerosols in the atmosphere. Based upon the Deep Blue results, our analyses indicate that during late April and May 2001 the smoke aerosols generated from fires over Siberia and near the Chinese border were seen to travel southward, reaching the Korean Peninsula and Sea of Japan. Due to the contribution from these smoke plumes, the coarse-mode dust signature was neutralized over the Sea of Japan in the April monthly

averaged Ångström exponent values when compared to those in March.

Generally speaking, the values of aerosol optical thickness in East Asia are higher in April 2001 for both coarse and fine mode particles than in March 2001. The satellite monthly aerosol maps shown in Fig. 12 demonstrate the complexity of the environment in East Asia in the spring. For most of China during this season, the lower tropospheric air masses constantly alternate between fine and coarse mode aerosols; sometimes they even overlap with each other at the same locations.

VII. SYNERGY OF MULTI-SATELLITE AEROSOL INFORMATION

To reduce the uncertainty in estimating climate forcing caused by tropospheric aerosols, it is important to produce the best quality climatology of aerosol properties by merging aerosol information obtained from the multiple satellite sensors that are currently available. However, different sensors have different temporal and spatial coverage as well as different data characteristics. Therefore, the advantages and disadvantages of information retrieved from each sensor must be understood before a consistent multi-platform aerosol database can be developed. In the first part of this section, we will first examine daily maps of aerosol properties for various aerosol-laden conditions as derived by SeaWiFS, MODIS, and MISR to give a flavor of the spatial and temporal coverage of each sensor. In the second part, we look at monthly mean aerosol properties. Because of the frequent cloudiness in this region during the spring, there are usually too few samples to form a statistically significant value that is representative of the entire month; this issue is particularly important for interpretation of the monthly mean aerosol properties calculated from each satellite sensor.

A. Dust Events

Fig. 13 shows daily maps of retrieved τ_a from MODIS and SeaWiFS using the Deep Blue algorithm as well as one of retrieved τ_a from MISR on April 6, 2001. The MISR

data used here are based on the version 17 dataset archived at the Langley Distributed Active Archive Center (DAAC) [5], [23]. Since both MISR and MODIS are onboard the Terra satellite, they are naturally collocated with a local equator crossing time of approximately 10:30 am. The 360 km wide cross-track MISR swath coincides with the center of the 2330 km wide cross-track MODIS swath. The local equator crossing time for SeaWiFS is near solar noon. Therefore, there is roughly a 1.5-hour time difference between the two satellite overpasses. Among the observations taken from these three sensors, MODIS provides the best spatial coverage, with almost no gaps between orbits at mid and high latitudes, while global coverage is achieved by SeaWiFS once every two days and by MISR once every 9 days.

A comparison of the retrieved τ_a distributions between MODIS and SeaWiFS shows that the dust front observed over Inner Mongolia (37° to 40° N, 104° to 110° E) in northwest China moved to the east between the overpass times. The dust plumes over Southern Mongolia were also seen to intensify and travel toward the east. These pointed dust plumes are indicative of potential dust sources in Southern Mongolia. The dust clouds over the Taklimakan desert, however, were only observed in the MODIS image, due to the orbital gaps in both SeaWiFS and MISR. Such spatial coverage plays an important role, statistically, in identifying source regions for such dust storms.

B.   Fine Mode Pollution Events

In contrast to the dust event on April 6, Fig. 14 shows that a thick layer of haze blanketed most of eastern China on April 2. An outflow of pollution plumes generated from this source region was also observed to extend into the Yellow Sea and Korean Peninsula. The corresponding retrieval of Ångström exponent values from MODIS and SeaWiFS (not shown here) ranged from 0.8 to 1.3, indicating that fine mode particles were dominant in this region. As shown in the MODIS true color image in Fig. 14a, these pollution clouds were generally confined within the boundary layer, since the mountains

in the vicinity seem to peek through the pollution layer. Such a pattern of thick haze over eastern China is very common during the winter and spring as a result of coal being burned to provide domestic heating. Because of the nature of its narrow swath, MISR misses this pollution event.

C.   Monthly Mean

We also compare monthly averages of the MODIS Deep Blue τ_a with those derived from the MODIS operational algorithm (collection 4) as well as τ_a derived from MISR and SeaWiFS data. The results for April 2001 are shown in Fig. 15. The black color in these τ_a maps represents the areas that do not have enough statistics to form the monthly averages due to constant cloud and snow/ice coverage. For the MODIS operational τ_a map (Fig. 15b), the black grid boxes are also indicative of the gaps due to bright reflecting surfaces such as arid and semi-arid regions. While an examination of these four satellite aerosol monthly maps indicates that a number of qualitative features in the regional aerosol distributions are similar among these sensors, such as persistent thick haze in the Sichuan basin and over eastern China as well as frequent dust clouds over the Taklimakan deserts and northwestern China, it also indicates that there are significant differences in the absolute values between these aerosol products.

It is apparent that much higher τ_a values are derived from the MODIS operational algorithm than either the MODIS Deep Blue or MISR products for the higher latitude zones that contain northern Mongolia and Russia. This is due to artifacts in the MODIS collection 4 data associated with cloud contamination and seasonal snow/ice coverage in this region. Elsewhere, MISR values are lower than the MODIS operational and Deep Blue values over the primary dust pathways in northern China as well as over the Taklimakan desert and the Gobi desert in Mongolia.

To help understand these differences, we use the AERONET monthly averages of τ_a as a benchmark. In Table 2 we compare AERONET values with those from the four sat-

ellite products for April 2001. Due to frequent cloudiness, the numbers of days used in calculating the AERONET monthly means were no more than 20 days at any of the four sites, as listed in the second column of Table 2. Despite different spatial resolution between the satellite grid box used in the monthly means ($1^{\circ} \times 1^{\circ}$) and ground-based measurements (single point representative of $\sim 0.1^{\circ}$), the monthly averages of MODIS Deep Blue τ_a agree well with the AERONET values for sites at Dunhuang and Inner Mongolia. For the Beijing site, the MODIS Deep Blue τ_a is lower than that of AERONET. However, an examination of the sunphotometer τ_a April time series at Beijing indicates that there were 4 days (out of 19 days) when daily τ_a values exceeded 2.0 at 500 nm. Among these 4 days, 3 (i.e., April 4, 10, and 28) had thick haze or heavy dust plumes occurring over Beijing in the early morning, with cloud cover developing by midday. Since the operational monthly mean AERONET values are computed based upon the daily averages available in the month and a daily mean is computed when more than three observations are available in a day [11], these extremely high values observed in-between the clouds were taken into account in the AERONET monthly mean. However, the satellite analyses could not take these conditions into account because of the cloud cover within the larger satellite pixel during the satellite overpass. We therefore recalculated the AERONET average for Beijing by excluding these 3 days and the result, as depicted in the value in parentheses below the operational value, is closer to the MODIS Deep Blue value.

For the Dalanzadgad site, the MODIS Deep Blue monthly τ_a is higher than the AERONET value in April 2001. We again examined the sampling issue and found that, for this site, there were no sunphotometer measurements made during the large dust storm events that occurred on April 6 and 29, which were clearly visible in the satellite imagery over southern Mongolia. Since the τ_a values at this site were generally small (around 0.1-0.2) for most days during April, a couple of days of enormous dust clouds

passing overhead with τ_a values of 2.0 or higher significantly enhanced the monthly mean in the satellite analysis. Indeed, the monthly τ_a was reduced from 0.47 to 0.20 when we recalculated the MODIS monthly τ_a using data from only the days that overlapped with the AERONET samples.

Although Fig. 15 shows some differences in the aerosol distribution patterns over eastern China, as seen by the MODIS operational and MODIS Deep Blue products, the monthly averages of τ_a at Beijing from these two data sets happen to be very close to one another as well as to the AERONET value that do not include the 3 dust/cloud events mentioned above. Both MISR and SeaWiFS values are slightly lower than the AERONET value at Beijing, as a result of missing a few high aerosol episodes due to the sampling rates of these two satellites. The April monthly value from the MODIS operational product over Inner Mongolia is higher than the AERONET and MODIS Deep Blue values. This is largely due to contamination associated with cloud and seasonal snow/ice coverage in this region in the MODIS collection 4 data. Once again, the MISR and SeaWiFS Deep Blue monthly values are smaller than the AERONET value over Inner Mongolia due to their limited sampling ability.

Since both Dunhuang and Dalanzadgad are located on bright-reflecting arid land, there are no aerosol retrievals from the MODIS operational algorithm. At Dalanzadgad the SeaWiFS Deep Blue monthly mean, which is similar to the MODIS Deep Blue value, after excluding the two dust events on April 4 and 29 from the analyses becomes closer to the AERONET and MISR monthly average, while at Dunhuang the MISR and SeaWiFS Deep Blue values are lower than the AERONET and MODIS Deep Blue values.

In general, MISR values are lower than the MODIS operational and Deep Blue values over East Asia in April 2001. This is probably due to the combination of a more conservative cloud screening scheme and limited sampling over the highly variable and transient environment discussed above. Due to frequent cloud cover in East Asia during

springtime, the sampling rate used to compute aerosol distribution and properties becomes a crucial factor in determining how representative the monthly means and their biases are for the aerosol climatology. Indeed, even using the same Deep Blue algorithm, the retrieved MODIS and SeaWiFS monthly averages deviate from one another, as a result of different sampling over the region. Because of this, even the monthly means from AERONET need to be used with caution for quantitative analysis.

VIII. CONCLUSIONS

Because of the urgent need to monitor dust outbreaks around the globe, there have been various techniques developed in recent years using a qualitative aerosol proxy such as the TOMS Aerosol Index (AI) derived from UV [9], [12] as well as other dust indices and dust enhanced products using infrared channels to detect the presence of dust plumes [19], [24]. However, with large uncertainties in surface emissivity (infrared) and surface reflectance (visible and UV), as well as uncertainties in vertical profiles of aerosol and water vapor, quantitative daily aerosol information is still lacking. For the first time, the Deep Blue algorithm provides comprehensive properties of aerosol optical thickness and Ångström exponent over high reflectance source regions using SeaWiFS- and MODIS-like sensors. This allows scientists to quantitatively track the evolution of dust and fine mode anthropogenic aerosols with only moderate sensitivity to uncertainties in aerosol plume height.

Using this technique we have studied the sources, pathways, and transport of dust and anthropogenic pollution aerosols in East Asia. Based upon the daily MODIS and SeaWiFS aerosol optical thickness and Ångström exponent maps derived from the Deep Blue algorithm, our analyses indicate that the major dust sources in East Asia are the Taklimakan desert, the Gobi desert in China and southern Mongolia, deserts in Inner Mongolia, and deserts in Horqin and Onqin Daga around 41° to 46° N and 110° to 125° E. These latter two sources are missing in the USGS dust erodible database presented in Fig.

5. This finding is consistent with the results of Gong *et al.* [6]. Various studies have developed dust source inventories based upon TOMS AI for input of dust transport models. However, because of its high sensitivity to dust altitude and its coarse spatial resolution, TOMS AI often misses dust plumes near sources in East Asia, particularly in March 2001. In contrast, the aerosol optical thickness derived from the Deep Blue algorithm is not very sensitive to the height of aerosol layers and thus can detect dust aerosols that reside close to the ground.

We have also compared the values of the Deep Blue aerosol optical thickness with the measurements collected at five different AERONET sites in China and Mongolia during the ACE-Asia experiment. Their locations range from the dust dominant site at Dunhuang to the aerosol compositionally complex site at Beijing. The collocated values of level 2 aerosol optical thickness derived from the Deep Blue algorithm are generally within 20–30% of those observed by the sunphotometers at all five sites. The comparisons of Ångström exponent values derived from the Deep Blue algorithm with those computed from the direct sun measurements at these five sites also demonstrate that the Deep Blue algorithm is capable of separating fine mode from coarse mode particles, even for the mixed aerosol environment such as in Beijing.

It is also noted that the satellite-retrieved single scattering albedo values from the Deep Blue algorithm exhibit different characteristics over different dust plumes. For example, the dust plumes over the Gobi desert in Mongolia (ω_0 ~0.87 at 412 nm) seem to be more absorbing compared to those transported from the Taklimakan desert and deserts in western Inner Mongolia (ω_0 ~0.94 at 412 nm). The spectral absorption of dust is believed linked to the iron oxide content within these particles [1] and may have implications on the fertilization of the ocean due to wind blown dust.

With the advent of advanced satellite sensors such as MODIS and MISR, high quality comprehensive aerosol climatology is becoming feasible for the first time, and studies

of the climate forcing due to tropospheric aerosols are now possible. However, each satellite measurement has advantages and disadvantages. While MODIS provides detailed spectral information from the blue part of the visible light spectrum to the IR, MISR offers comprehensive angular information in a narrow swath of reflected sunlight at three visible channels and one near-infrared channel using nine cameras. This angular information is important for separating the surface contribution from the atmosphere, determining aerosol phase function, and inferring cloud and aerosol plume heights, particularly over arid and semi-arid surfaces [23]. However, in a region where the dynamic range of aerosol loading is large, such as East Asia in the spring, the lack of spatial coverage significantly impacts the resulting monthly average in the satellite retrieved aerosol climatology. Only when the different characteristics of each satellite are understood and taken into account, as we have done, can a synergy of multi-sensor aerosol information be used to create accurate tropospheric aerosol climatology for use in climate forcing studies.

ACKNOWLEDGMENT

R<small>EFERENCES</small>

[1]   S. C. Alfaro, S. Lafon, J. L. Rajot, P. Formenti, A. Gaudichet, and M. Maille, "Iron oxides and light absorption by pure desert dust: An experimental study," *J. Geophys. Res.*, vol. 109, D08208, doi:10.1029/2003JD004374, 2004.

[2]   M. Chin, P. Ginoux, R. Lucchesi, B. Huebert, R. Weber, T. Anderson, S. Masonis, B. Blomquist, A. Bandy, and D. Thornton, "A global aerosol model forecast for the ACE Asia field experiment," *J. Geophys. Res.*, vol. 108(D23), 8654, doi:10.1029/ 2003JD003642, 2003.

[3]   D. A. Chu, Y. J. Kaufman, J-D Chern, J-M Mao, C. Li, and B. N. Holben, "Global monitoring of air pollution over land from EOS-Terra MODIS," *J. Geophys. Res.*, vol. 108, 4661, doi:10.1029/2002JD003179, 2003.

[4]   J. V. Dave, "Development of programs for computing characteristics of ultraviolet radiation," technical report, Vector Case, IBM Corp., Fed. Syst. Div., Gaithersburg, MD., 1972.

[5]   D. J. Diner, J. V. Martonchik, R. A. Kahn, B. Pinty, N. Gobron, D. L. Nelson, and B. N. Holben, "Using angular and spectral shape similarity constraints to improve MISR aerosol and surface retrievals over land," *Rem. Sens. Environ.*, vol. 94, pp. 155-171, 2005.

[6]   S. L. Gong, X. Y. Zhang, T. L. Zhao, I. G. McKendry, D. A. Jaffe, and N. M. Lu, "Characterization of soil dust aerosol in China and its transport and distribution during 2001 ACE-Asia: 2. Model simulation and validation," *J. Geophys. Res.*, vol. 108(D9), 4262, doi:10.1029/2002JD002633, 2003.

[7]   F. E. Grousset, P. Ginoux, A. Bory, P. E. Biscaye, "Case study of a Chinese dust plume reaching the French Alps," *Geophys. Res. Lett.*, vol. 30, no. 6, 1277, doi: 10.1029/2002GL016833, 2003.

[8]   J. Haywood, and O. Bougher, "Estimates of the direct and indirect radiative forcing

due to tropospheric aerosols: a review," *Rev. Geophys.*, vol. 38, pp. 513-543, 2000.

[9]   J. R. Herman, P. K. Bhartia, O. Torres, N. C. Hsu, C. J. Seftor, and E. Celarier, "Global distribution of UV-absorbing aerosols from Nimbus-7/TOMS data," *J. Geophys. Res.*, vol. 102, pp. 16911-16922, 1997.

[10]   J. R. Herman, and E. A. Celarier, "Earth surface reflectivity climatology at 340-380 nm from TOMS data," *J. Geophys. Res.*, vol. 102, pp. 28003-28011, 1997.

[11]   B. N. Holben, D. Tanré, A. Smirnov, T. F. Eck, I. Slutsker, N. Abuhassan, W. W. Newcomb, J. Schafer, B. Chatenet, F. Lavenue, Y. J. Kaufman, J. Vande Castle, A. Setzer, B. Markham, D. Clark, R. Frouin, R. Halthore, A. Karnieli, N. T. O'Neill, C. Pietras, R. T. Pinker, K. Voss, and G. Zibordi, "An emerging ground-based aerosol climatology: Aerosol optical depth from AERONET," *J. Geophys. Res.*, vol. 106, pp. 12067-12097, 2001.

[12]   N. C. Hsu, J. R. Herman, P. K. Bhartia, C. J. Seftor, O. Torres, A. M. Thompson, J. F. Gleason, T. F. Eck, and B. N. Holben, "Detection of biomass burning smoke from TOMS measurements," *Geophys. Res. Lett.*, vol. 23, pp. 745-748, 1996.

[13]   N. C. Hsu, J. R. Herman, and C. Weaver, "Determination of radiative forcing of Saharan dust using combined TOMS and ERBE data," *J. Geophys. Res.*, vol. 105, pp. 20649-20661, 2000.

[14]   N. C. Hsu, S. C. Tsay, M. D. King, and J. R. Herman, "Aerosol properties over bright-reflecting source regions," *IEEE Trans. Geosci. Remote Sens.*, vol. 42, 557-569, 2004.

[15]   B. J. Huebert, T. Bates, P. B. Russell, G. Shi, Y. J. Kim, K. Kawamura, G. Carmichael, and T. Nakajima, "An overview of ACE-Asia: Strategies for quantifying the relationships between Asian aerosols and their climatic impacts," *J. Geophys. Res.*, vol. 108(D23), 8633, doi:10.1029/2003JD003550, 2003.

[16]   Y. J. Kaufman, D. Tanré, L. A. Remer, E. F. Vermote, D. A. Chu, and B. N. Hol-

ben, "Remote sensing of tropospheric aerosol from EOS-MODIS over the land using dark targets and dynamic aerosol models," *J. Geophys. Res.*, vol. 102, pp. 17051-17067, 1997.

[17] Y. J. Kaufman, A. Wald, L. A. Remer, B. C. Gao, R. R. Li, and L. Flynn, "Remote sensing of aerosol over the continents with the aid of a 2.2 μm channel," *IEEE Trans. Geosci. Remote Sens.*, vol. 35, pp. 1286-1298, 1997.

[18] M. D. King, Y. J. Kaufman, D. Tanré, and T. Nakajima, "Remote sensing of tropospheric aerosols from space: Past, present and future," *Bull. Amer. Meteor. Soc.*, vol. 80, pp. 2229-2259, 1999.

[19] M. Legrand, A. Plana-Fattori, and C. N'doumé, "Satellite detection of dust using the IR imagery of Meteosat 1. Infrared difference dust index," *J. Geophys. Res.*, vol. 106(D16), pp. 18251-1274, 2001.

[20] J. Liu, H. Tian, M. Liu, D. Zhuang, J. M. Melillo, and Z. Zhang, "China's changing landscape during the 1990s: Large-scale land transformations estimated with satellite data," *Geophys. Res. Lett.*, vol. 32, L02405, doi:10.1029/2004GL021649, 2005.

[21] J. J. Liu, Z. Li, Y.-L. Qiao, Y. J. Liu, and Y. X. Zhang, "A new method for cross-calibration of two satellite sensors," *Int. J. Remote Sens.*, vol. 25(23), pp. 5267–5281, 2004.

[22] M. Liu, D. L. Westphal, S. Wang, A. Shimizu, N. Sugimoto, J. Zhou, and Y. Chen, "A high-resolution numerical study of the Asian dust storms of April 2001," *J. Geophys. Res.*, vol. 108(D23), 8653, doi:10.1029/2002JD003178, 2003.

[23] J. V. Martonchik, D. J. Diner, R. Kahn, B. Gaitley, and B. N. Holben, "Comparison of MISR and AERONET aerosol optical depths over desert sites," *Geophys. Res. Lett.*, vol. 31, L16102, doi:10.1029/2004GL019807, 2004.

[24] S. D. Miller, "A consolidated technique for enhancing desert dust storms with MODIS," *Geophys. Res. Lett.*, vol. 30(20), 2071, doi:10.1029/ 2003GL018279,

2003.

[25] M. I. Mishchenko, Lacis, A.A., and Travis, L.D. "Errors introduced by the neglect of polarization in radiance calculations for Rayleigh scattering atmospheres," *J. Quant. Spectrosc. Radiat. Transfer*, vol. 51, pp. 491-510, 1994.

[26] D. Tanré, and M. Legrand, "On the satellite retrieval of Saharan dust optical thickness over land: two different approaches," *J. Geophys. Res.*, vol. 96, pp. 5221-5227, 1991.

[27] D. Tanré, E. F. Vermote, B. N. Holben, and Y. J. Kaufman, "Satellite aerosol retrieval over land surfaces using the structure functions," In: IGARSS '92, Proceedings of the 12th annual Int. Geosci Remote Sens. Symposium, vol. 2, pp. 1474-1477, 1992.

[28] D. M. Tratt, R. J. Frouin, and D. L. Westphal, "April 1998 Asian dust event: A southern California perspective," *J. Geophys. Res.*, vol. 106, pp. 18371–18379, 2001.

[29] I. Uno, G. R. Carmichael, D. G. Streets, Y. Tang, J. J. Yienger, S. Satake, Z. Wang, Jung-Hun Woo, S. Guttikunda, M. Uematsu, K. Matsumoto, H. Tanimoto, K. Yoshioka, and T. Iida, "Regional chemical weather forecasting system CFORS: Model descriptions and analysis of surface observations at Japanese island stations during the ACE-Asia experiment," *J. Geophys. Res.*, vol. 108(D23), 8668, doi:10.1029/ 2002JD002845, 2003.

N. Christina Hsu received the B.S. degree from the National Taiwan University, Taipei, R.O.C., in Taipei, Taiwan in 1984, and the Ph.D. degree from the Georgia Institute of Technology, Atlanta, in 1991, both in atmospheric sciences.

She joined Goddard Space Flight Center (GSFC), Greenbelt, MD, as a Physical Scientist in the Climate and Radiation Branch, Laboratory for Atmospheres, in February 2005. From 2001 to 2005 she was an Associate Research Scientist in the Goddard Earth Sciences and Technology Center, University of Maryland, Baltimore County. She is a member of the EOS MODIS, CERES, and TOMS Science Teams, where her focus is on the properties of aerosols in both the UV and visible spectra and determination of the radiative forcing due to tropospheric aerosols. Her research experience includes aerosol-climate interaction studies and development of near-real-time satellite retrieval of aerosols using SeaWiFS and MODIS measurements over ocean and over bright-reflecting dust source regions for field campaigns.

Si-Chee Tsay received the B.S. degree from the National Taiwan University, Taipei, Taiwan, R.O.C. in 1977, and the M.S. and Ph.D. degrees from the University of Alaska, Fairbanks, in 1982 and 1986, respectively, all in atmospheric sciences.

He joined Goddard Space Flight Center as a Physical Scientist in the Climate and Radiation Branch, Laboratory for Atmospheres, in August 1994. From 1990 to 1994, he was a Visiting Scientist in the Universities Space Research Association, and from 1986 to 1990, he was a Research Scientist in the Department of Atmospheric Science, Colorado State University, Fort Collins. He has been an Adjunct Professor with the Earth Systems Science Interdisciplinary Center, University of Maryland, College Park, since 2002. He is a Principal Investigator in many NASA and other federal agency projects and is currently the EOS/Terra Deputy Project Scientist.

Michael D. King (M'01–SM'03) received the B.A. degree in physics from Colorado

College, Colorado Springs, in 1971, and the M.S. and Ph.D. degrees in atmospheric sciences from the University of Arizona, Tucson, in 1973 and 1977, respectively.

In January 1978 he joined NASA Goddard Space Flight Center, Greenbelt, MD, and is currently Senior Project Scientist of NASA's Earth Observing System (EOS), a position he has held since 1992. He is a member of the MODIS Science Team where he has primary responsibility for developing the cloud optical and microphysical property and Level-3 algorithms. His research experience includes conceiving, developing, and operating multispectral scanning radiometers from a number of aircraft platforms in field experiments ranging from arctic stratus clouds to smoke from the Kuwait oil fires in the Persian Gulf and biomass burning in Brazil and southern Africa.

Dr. King is a Fellow of the American Geophysical Union (AGU) and American Meteorological Society (AMS), recipient of the AMS Verner E. Suomi Award for significant and fundamental contributions to remote sensing and radiative transfer, and a member of the U.S. National Academy of Engineering.

Jay R. Herman received the B.S. degree from the Clarkson College, Potsdam, NY in 1959, and the M.S. and Ph.D. degree from the Pennsylvania State University, University Park, in 1963 and 1965, respectively, all in physics.

He joined NASA Goddard Space Flight Center in 1965 and is currently Principal Investigator of the TOMS UV and aerosol projects. His research experience includes ion chemistry, earth ionosphere, planetary ionospheres, radio wave propagation in plasmas, stratospheric chemistry and modeling, radiative transfer, atmospheric spectroscopy, UV solar flux measurements, ozone inversion algorithms, long-term ozone trend analysis, volcanic aerosols, and physical oceanography.

TABLE I
GROUND-BASED AEROSOL INFORMATION USED IN THIS ANALYSIS FROM AERONET

Location	Lat., Long.	Elevation (m)	Months[a]
Dunhuang	40.04°N, 94.79°E	1300	AM'01
Dalanzadgad	43.58°N, 104.42°E	1470	MAM'01
Yulin	38.28°N, 109.72°E	1080	May'01
Inner Mongolia	42.68°N, 115.95°E	1343	AM'01
Beijing	39.98°N, 116.38°E	92	MAM'01

[a]MAM'01 represents data from the months of March, April, and May of 2001.

TABLE II
AEROSOL PROPERTY MONTHLY STATISTICS FOR APRIL 2001

Location	Number of Days	AERONET τ_a / α	MODIS Deep Blue τ_a	MODIS Operational τ_a	MISR τ_a	SeaWiFS Deep Blue τ_a / α
Beijing	19	1.01 / 0.78 (0.76/0.79)**	0.78	0.78	0.61	0.64 / 0.76
Inner Mongolia	11	0.45 / 0.82	0.52	0.99	0.26	0.25 / 0.83
Dunhuang	17	1.00 / 0.12	1.08	N/A	0.62	0.78 / 0.34
Dalanzadgad	20	0.15 / 1.12	0.47 (0.20)*	N/A	0.20	0.48 / 0.75 (0.22/0.83)*

*The numbers inside the parentheses indicate sampling MODIS/SeaWiFS data on the same days as AERONET measurements.

**The numbers inside the parentheses depict the monthly mean computed without including April 4, 10, and 28 when cloud cover was present over most of the mid-days.

FIGURE LEGENDS

Fig. 1.   Time series of TOMS aerosol index composite during April 2001, showing long-range transport of Asian dust across the Pacific reaching as far as the east coast of the United States.

Fig. 2.   (Top) Values of spectral surface reflectance for arid regions (line with asterisks scaled on the right axis) and single scattering albedo (lines with open circles and closed circles scaled on the left axis for D1 and D2 dust models, respectively) as inputs for the theoretical simulations. The value of co-single scattering albedo is equivalent to unity minus single scattering albedo. (Bottom) Magnitudes of the calculated Efficiency Index for detecting the presence of aerosols as a function of wavelength at two different view zenith angles of 0° (solid lines) and 60° (dashed lines). The corresponding values for D1 and D2 models are represented by open circles and closed circles, respectively. The aerosol optical thickness $\tau_a = 1$, solar zenith angle $\theta_0 = 20^o$ and relative azimuth angle $\phi = 120^o$.

Fig. 3.   Apparent reflectances (upper panel) and the corresponding errors in the retrieved τ_a and ω_0 (lower panel) due to uncertainty in aerosol height as a function of wavelength from 340 to 670 nm and for the D2 aerosol model. (a) The dashed lines represent apparent reflectances for $\tau_a = 0.5$, 1.0, and 1.5 when the aerosol plume is located at 3 km, as assumed in the Deep Blue algorithm. The gray solid and chain-dashed lines depict the reflectances for $\tau_a = 1.0$, but with aerosol plumes located at 1 and 5 km, respectively. (b) Simulated apparent reflectance as a function of wavelength for $\tau_a = 1.0$ and $\omega_0 = 0.91$, 0.94, and 0.97 (dashed lines) for a plume height of 3 km. Reflectances for the same plumes with $\tau_a = 1.0$ and $\omega_0 = 0.94$, but located at 1 and 5 km, are also displayed by gray solid and chain-dashed lines. (Bottom panel) Resulting errors in the computed (c) τ_a and (d) ω_0 associated with plume heights resided at 1 and 5 km by

using the lookup tables calculated assuming 3 km.

Fig. 4.   Flow chart of the Deep Blue algorithm.

Fig. 5.   A graphic image of the pre-calculated land surface reflectance database used in the Deep Blue algorithm at the resolution of 0.1^o latitude by $0.1°$ longitude for spring 2001 at (a) 412 nm from SeaWiFS and (c) 650 nm channel from MODIS. The white color represents data gaps due to the persistent presence of clouds or seasonal snow/ice cover. The values of surface reflectance at 380 nm from TOMS at 1° latitude by 1.25^o longitude resolution and the USGS dataset of dust erodible fraction (0-1) in land cover over East Asia at 9 km grid resolution are also depicted in (b) and (d), respectively.

Fig. 6.   Daily maps of aerosol optical thickness at 490 nm (top), Ångström exponent (412-490 nm) (middle), and single scattering albedo at 412 nm (bottom) retrieved from SeaWiFS during April 6-7, 2001. The black/gray areas represent either orbital gaps or regions covered by clouds or snow/ice.

Fig. 7.   Comparisons of spectral reflectance taken over two different dust plumes on April 6, 2001 from SeaWiFS: the north plume in Mongolia (43° to 44°N and 105° to 106°E) (line with closed circles), and the south plume over Inner Mongolia province (38° to 39°N, 104° to 105°E) in China (line with open circles). The corresponding spectral reflectances over the same regions observed during clear days are also superimposed as dashed lines.

Fig. 8.   The geolocations of the five AERONET sites during ACE-Asia, superimposed with the surface elevation database from ETOPO5.

Fig. 9.   The values of aerosol optical thickness at 500 nm vs. Ångström exponent measured by AERONET sunphotometers located at (a) Dunhuang, (b) Inner Mongolia, and (c) Dalanzadgad during April 2001.

Fig. 10. Comparisons of aerosol optical thickness retrieved from the SeaWiFS Deep

Blue algorithm during March-May 2001 with those from AERONET sunpho-

tometers located at (a) Dunhuang, (b) Inner Mongolia, (c) Yulin, and (d) Dalan-

zadgad. The solid lines are the one-to-one lines between the satellite retrieved

aerosol optical thickness and sunphotometer measured values. The dashed line

represents the 20% differences; the chain-dashed line represents 30% differ-

ences.

Fig. 11. (a) The values of aerosol optical thickness vs. Ångström exponent at Beijing

from AERONET. (b) Comparisons of satellite retrieved τ_a at 490 nm vs. τ_a at

500 nm from AERONET at Beijing. (c) Comparisons of satellite retrieved

Ångström exponent (412-490 nm) vs. those derived from AERONET at Beijing.

Fig. 12. Monthly average of aerosol optical thickness at 500 nm and Ångström exponent

(412-490 nm) retrieved from the SeaWiFS Deep Blue algorithm for each $1^o \times 1^o$

grid box in East Asia for March and April 2001. The black color represents the

region where there are not enough samples for calculation of the monthly mean

due to the presence of clouds or seasonal snow/ice cover.

Fig. 13. (a) Terra/MODIS true color image taken on April 6, 2001 reveals several dust

storms over Mongolia and northwestern China. The corresponding daily level 2

maps of aerosol optical thickness retrieved from Deep Blue algorithm at mid-

visible wavelength (i.e., 550 nm) are shown using (b) SeaWiFS and (c) MODIS

reflectance measurements. The aerosol optical thickness from operational MISR

products on the same day is also depicted in (d).

Fig. 14. The extent of a severe pollution event over eastern China on April 2, 2001 is

captured by (a) Terra/MODIS true color image. (b) and (c) display the corre-

sponding level 2 distributions of aerosol optical thickness retrieved from Deep

Blue algorithm at mid-visible wavelength (i.e., 550 nm) using SeaWiFS and

MODIS measurements taken from this day, respectively. (d) Image of the aero-

sol optical thickness values derived from the operational algorithm for April 2 from MISR, which is also aboard on Terra, is shown over the same region.

Fig. 15.   Monthly average aerosol optical thickness retrieved at mid-visible wavelength (i.e., 550 nm) from (a) the MODIS Deep Blue algorithm, (b) the MODIS collection 4 operational product, (c) the SeaWiFS Deep Blue algorithm, and (d) the MISR aerosol product for each $1^o \times 1^o$ grid box in East Asia for April 2001. The black color represents data gaps due to the presence of clouds or seasonal snow/ice cover (e.g., Deep Blue MODIS and SeaWiFS as well as MISR) and/or due to the bright reflecting surfaces (e.g., operational MODIS).   Both the MODIS and SeaWiFS Deep Blue monthly means use criteria that require a minimum sample number of six cloud-free days, while the ones from MISR and MODIS collection 4 do not adopt such criteria.

Figure 1. Time series of TOMS aerosol index composite during April 2001, showing long-range transport of Asian dust across the Pacific reaching as far as the east coast of the United States.
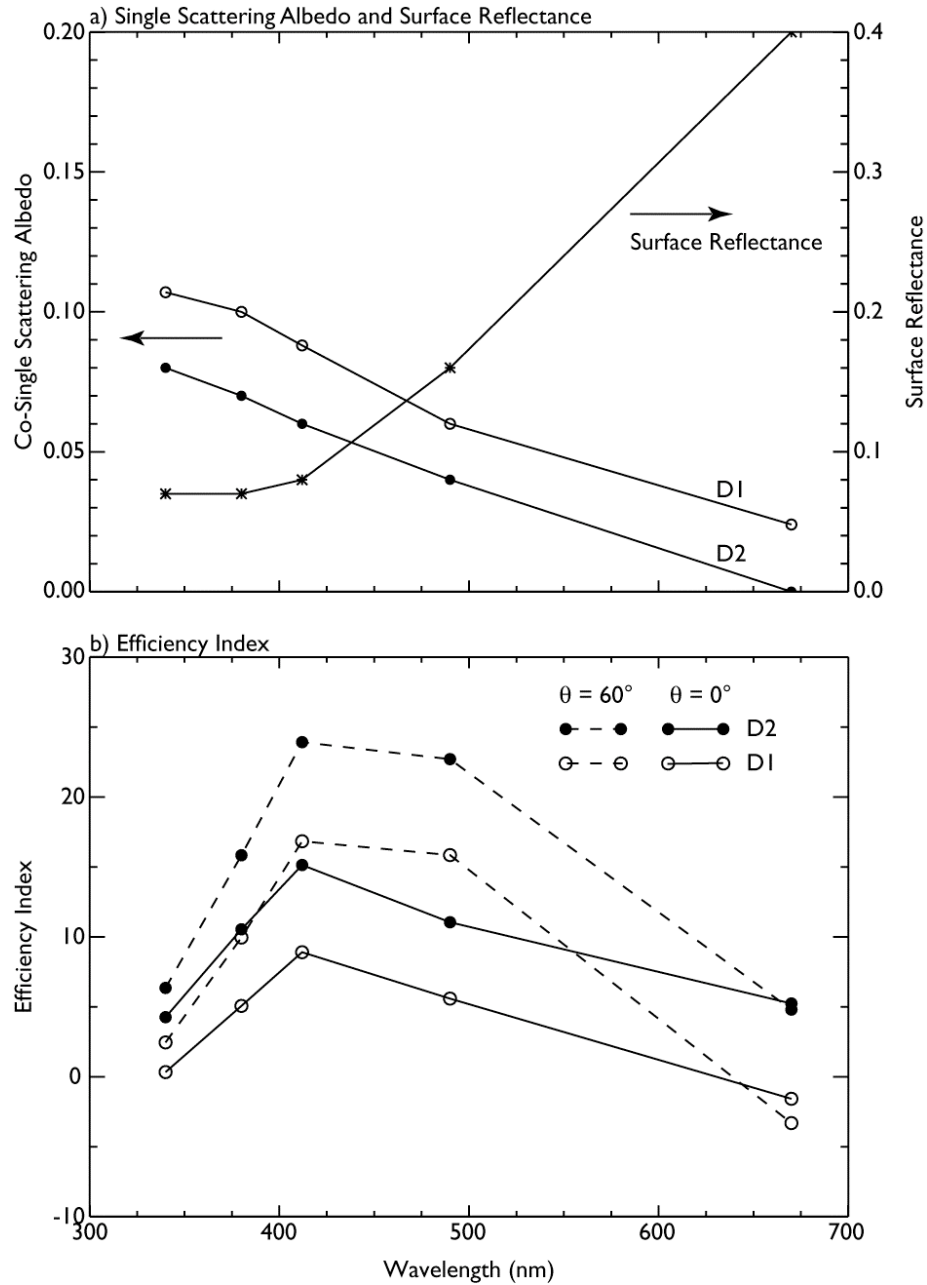
Figure 2.   (Top) Values of spectral surface reflectance for arid regions (line with asterisks scaled on the right axis) and single scattering albedo (lines with open circles and closed circles scaled on the left axis for D1 and D2 dust models, respectively) as inputs for the theoretical simulations. The value of co-single scattering albedo is equivalent to unity minus single scattering albedo. (Bottom) Magnitudes of the calculated Efficiency Index for detecting the presence of aerosols as a function of wavelength at two different view zenith angles of 0° (solid lines) and 60° (dashed lines). The corresponding values for D1 and D2 models are represented by open circles and closed circles, respectively. The aerosol optical thickness $\tau_a = 1$, solar zenith angle $\theta_0 = 20^o$ and relative azimuth angle $\phi = 120^o$.

Figure 3.   Apparent reflectances (upper panel) and the corresponding errors in the retrieved τ_a and ω_0 (lower panel) due to uncertainty in aerosol height as a function of wavelength from 340 to 670 nm and for the D2 aerosol model. (a) The dashed lines represent apparent reflectances for τ_a = 0.5, 1.0, and 1.5 when the aerosol plume is located at 3 km, as assumed in the Deep Blue algorithm. The gray solid and chain-dashed lines depict the reflectances for τ_a = 1.0, but with aerosol plumes located at 1 and 5 km, respectively. (b) Simulated apparent reflectance as a function of wavelength for τ_a = 1.0 and ω_0 = 0.91, 0.94, and 0.97 (dashed lines) for a plume height of 3 km. Reflectances for the same plumes with τ_a = 1.0 and ω_0 = 0.94, but located at 1 and 5 km, are also displayed by gray solid and chain-dashed lines. (Bottom panel) Resulting errors in the computed (c) τ_a and (d) ω_0 associated with plume heights resided at 1 and 5 km by using the lookup tables calculated assuming 3 km.

Figure 4.   Flow chart of the Deep Blue algorithm.

Figure 5.   A graphic image of the pre-calculated land surface reflectance database used in the Deep Blue algorithm at the resolution of 0.1° latitude by 0.1° longitude for spring 2001 at (a) 412 nm from SeaWiFS and (c) 650 nm channel from MODIS. The white color represents data gaps due to the persistent presence of clouds or seasonal snow/ice cover. The values of surface reflectance at 380 nm from TOMS at 1° latitude by 1.25° longitude resolution and the USGS dataset of dust erodible fraction (0-1) in land cover over East Asia at 9 km grid resolution are also depicted in (b) and (d), respectively.
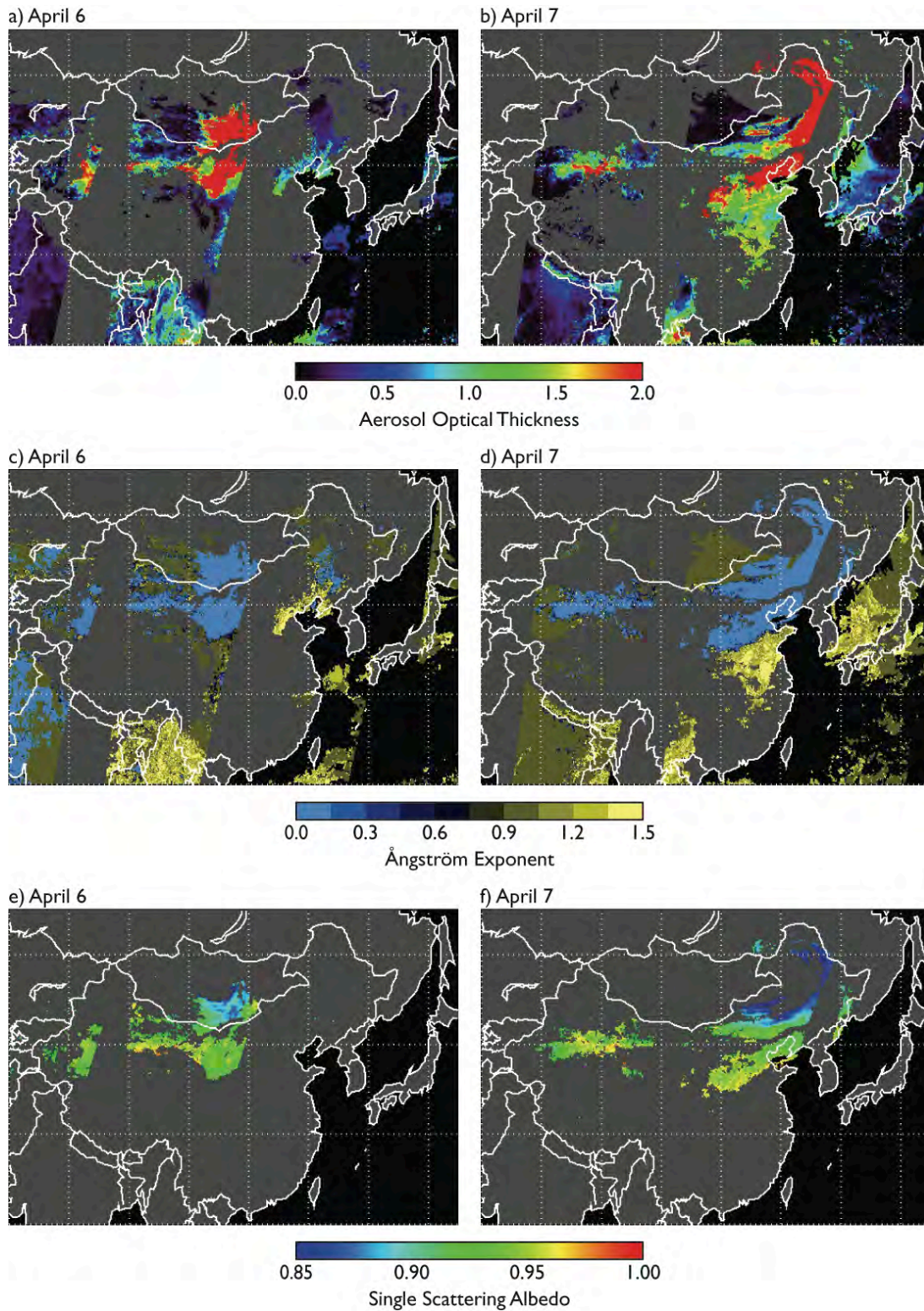
Figure 6.   Daily maps of aerosol optical thickness at 490 nm (top), Ångström exponent
(412-490 nm) (middle), and single scattering albedo at 412 nm (bottom) re-
trieved from SeaWiFS during April 6-7, 2001. The black/gray areas repre-
sent either orbital gaps or regions covered by clouds or snow/ice.
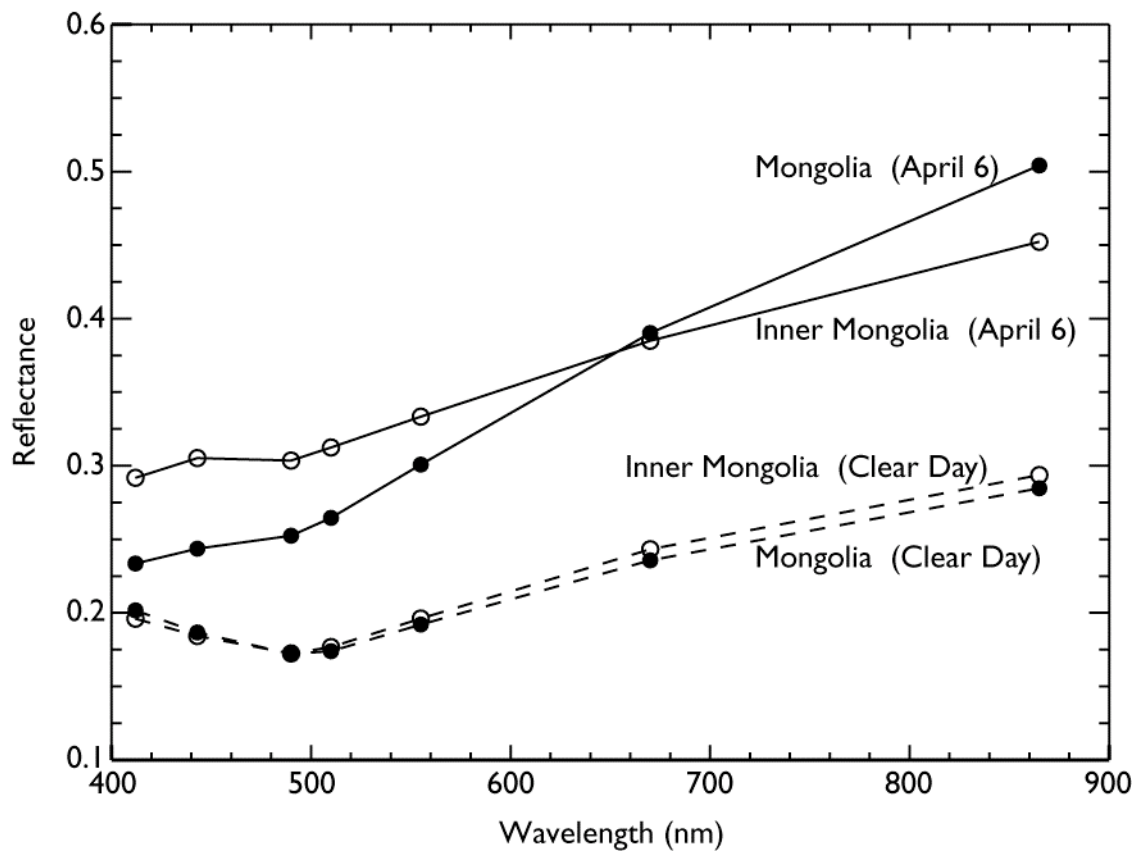
Figure 7.   Comparisons of spectral reflectance taken over two different dust plumes on April 6, 2001 from SeaWiFS: the north plume in Mongolia (43° to 44°N and 105° to 106°E) (line with closed circles), and the south plume over Inner Mongolia province (38° to 39°N, 104° to 105°E) in China (line with open circles). The corresponding spectral reflectances over the same regions observed during clear days are also superimposed as dashed lines.
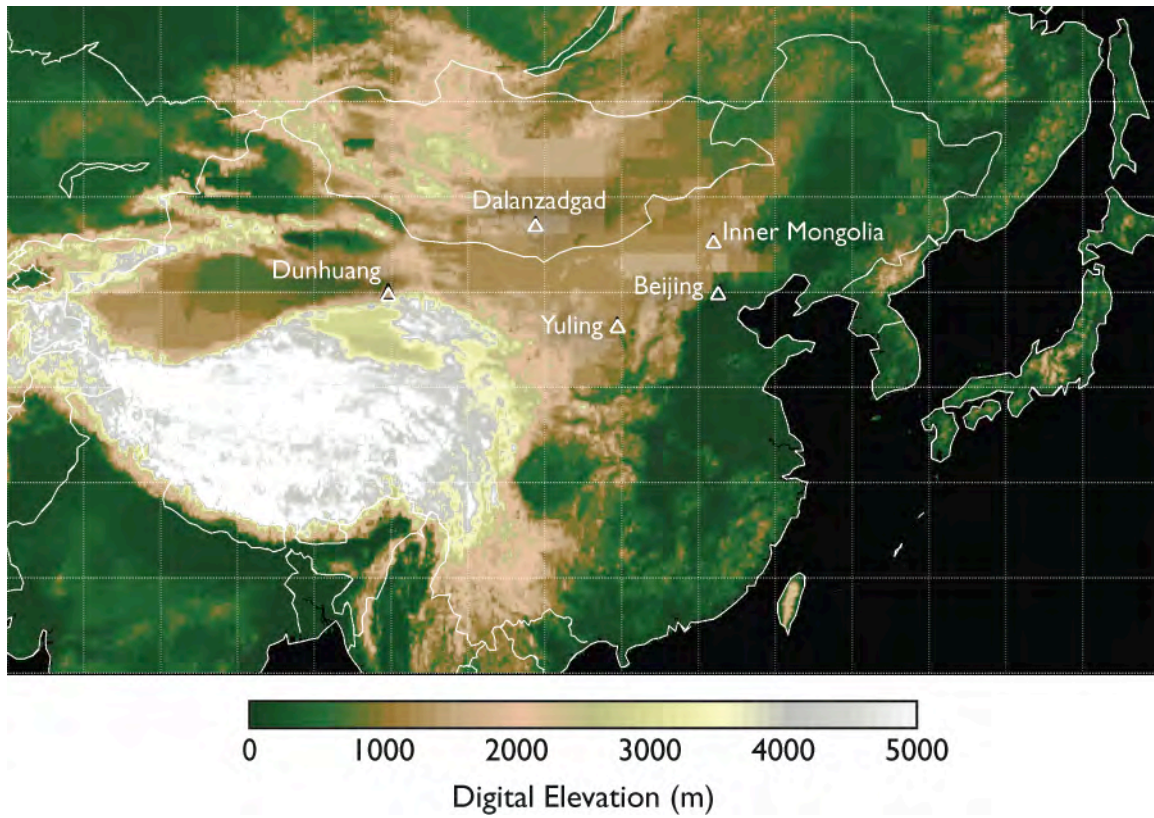
Figure 8.   The geolocations of the five AERONET sites during ACE-Asia, superimposed with the surface elevation database from ETOPO5.
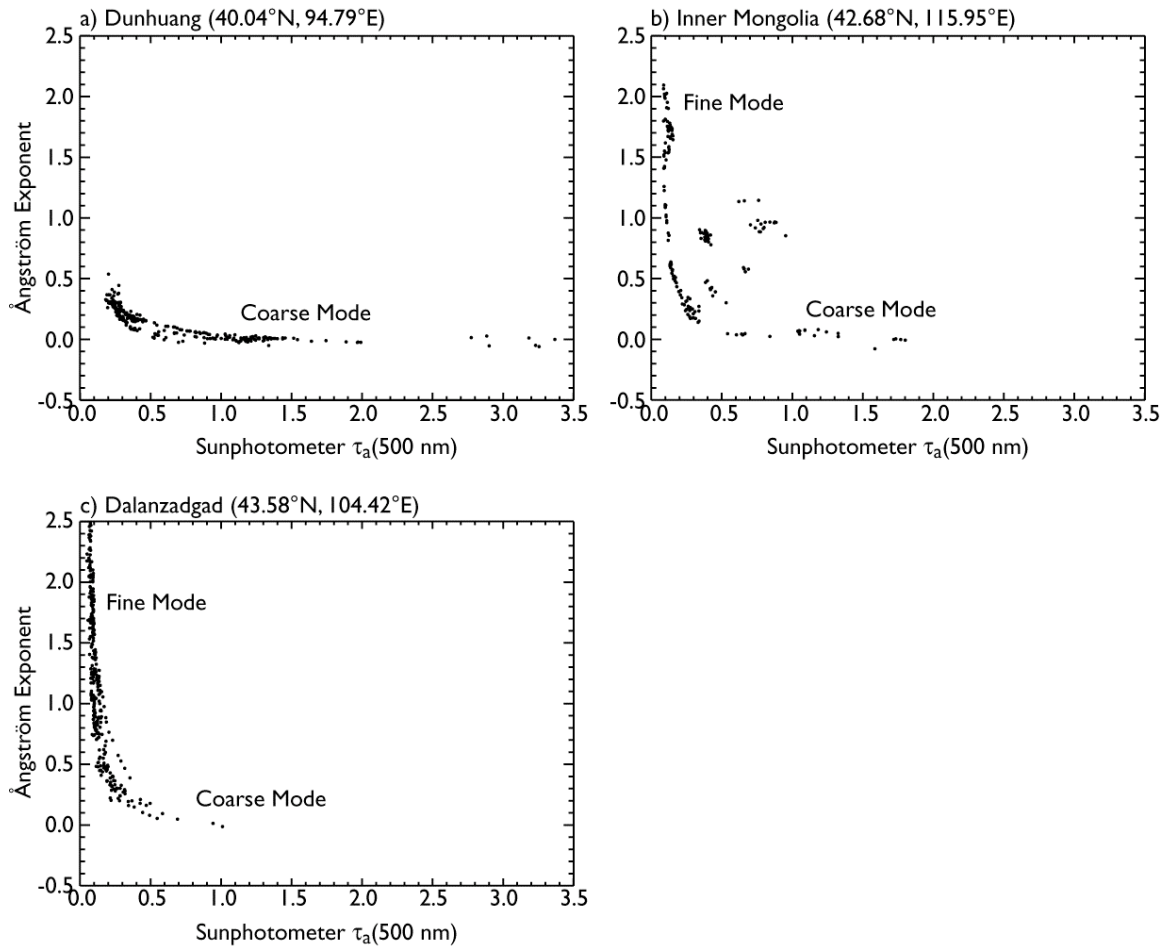
Figure 9. The values of aerosol optical thickness at 500 nm vs. Ångström exponent measured by AERONET sunphotometers located at (a) Dunhuang, (b) Inner Mongolia, and (c) Dalanzadgad during April 2001.
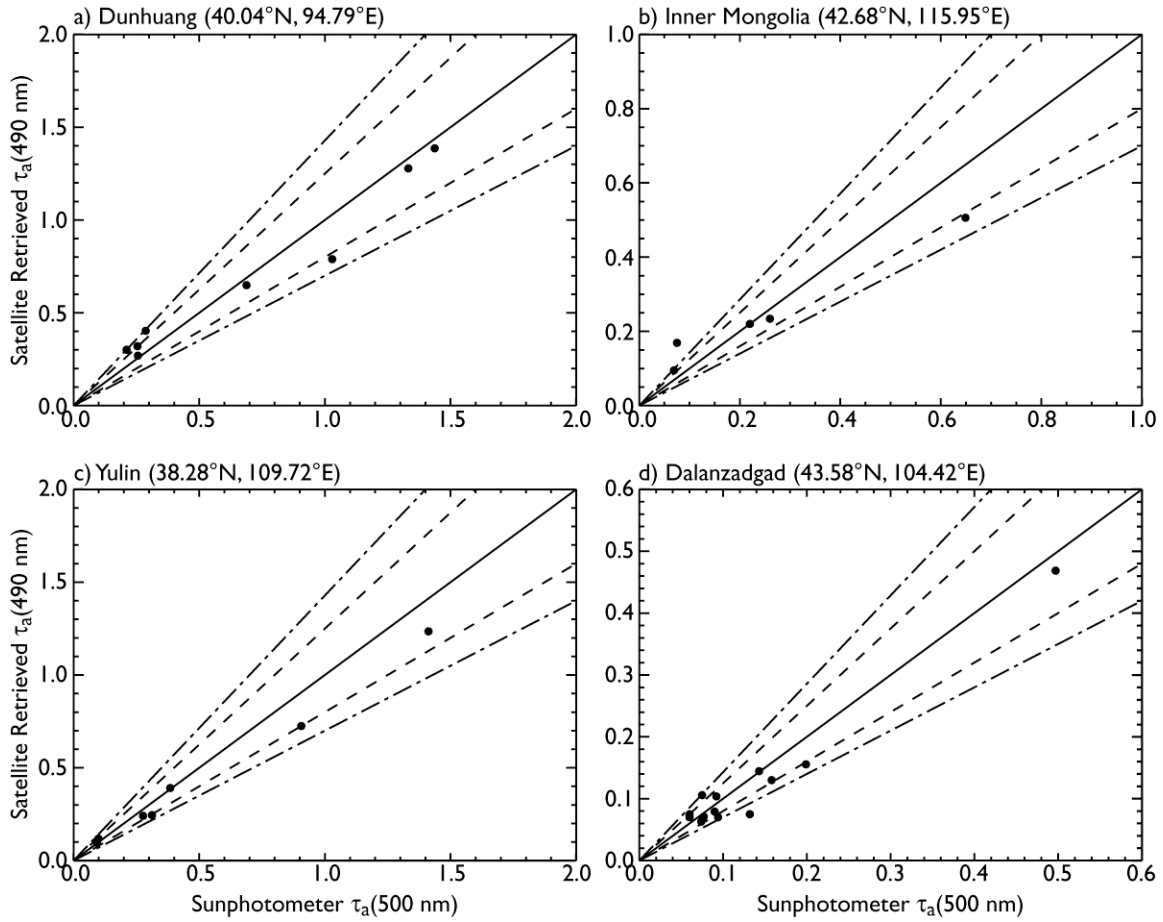
Figure 10. Comparisons of aerosol optical thickness retrieved from the SeaWiFS Deep Blue algorithm during March-May 2001 with those from AERONET sunphotometers located at (a) Dunhuang, (b) Inner Mongolia, (c) Yulin, and (d) Dalanzadgad. The solid lines are the one-to-one lines between the satellite retrieved aerosol optical thickness and sunphotometer measured values. The dashed line represents the 20% differences; the chain-dashed line represents 30% differences.
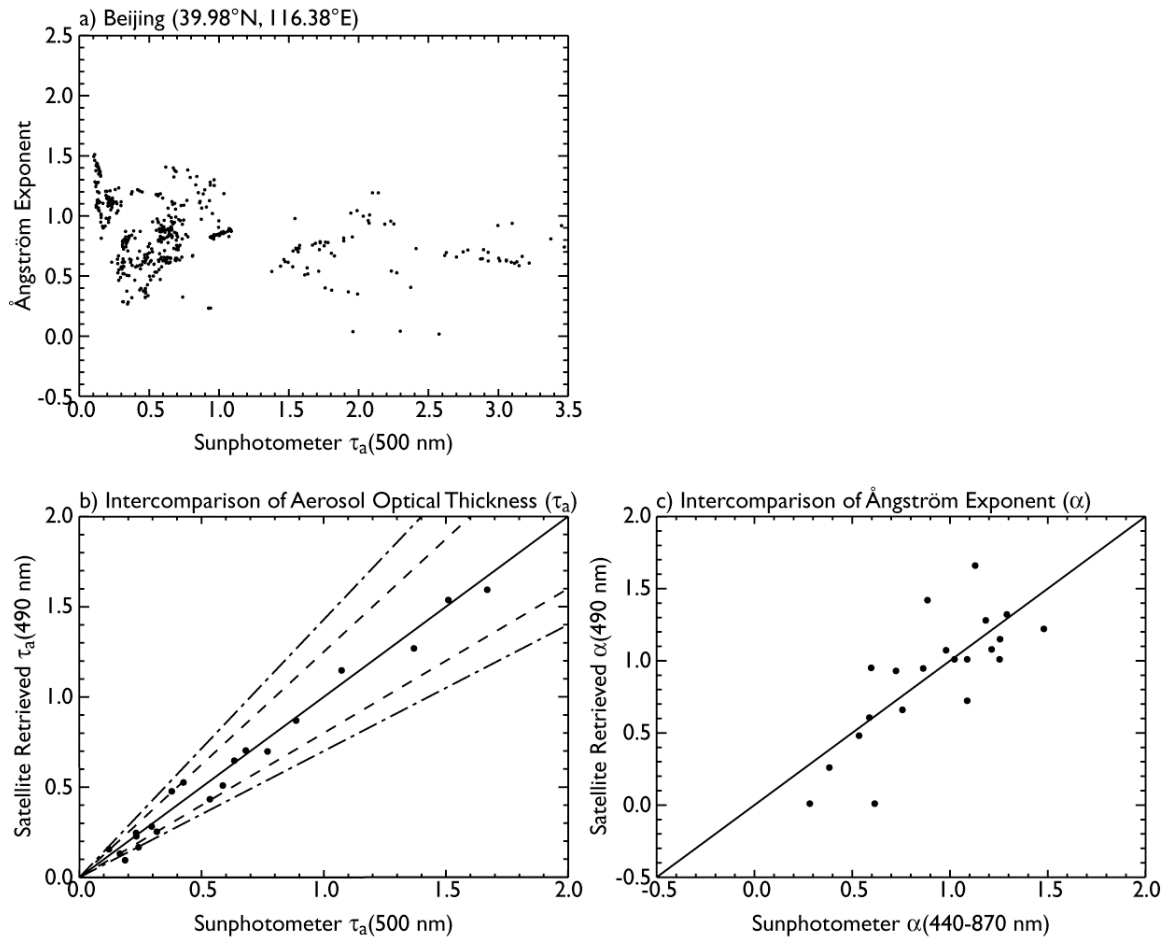
Figure 11. (a) The values of aerosol optical thickness vs. Ångström exponent at Beijing from AERONET. (b) Comparisons of satellite retrieved τ_a at 490 nm vs. τ_a at 500 nm from AERONET at Beijing. (c) Comparisons of satellite retrieved Ångström exponent (412-490 nm) vs. those derived from AERONET at Beijing.
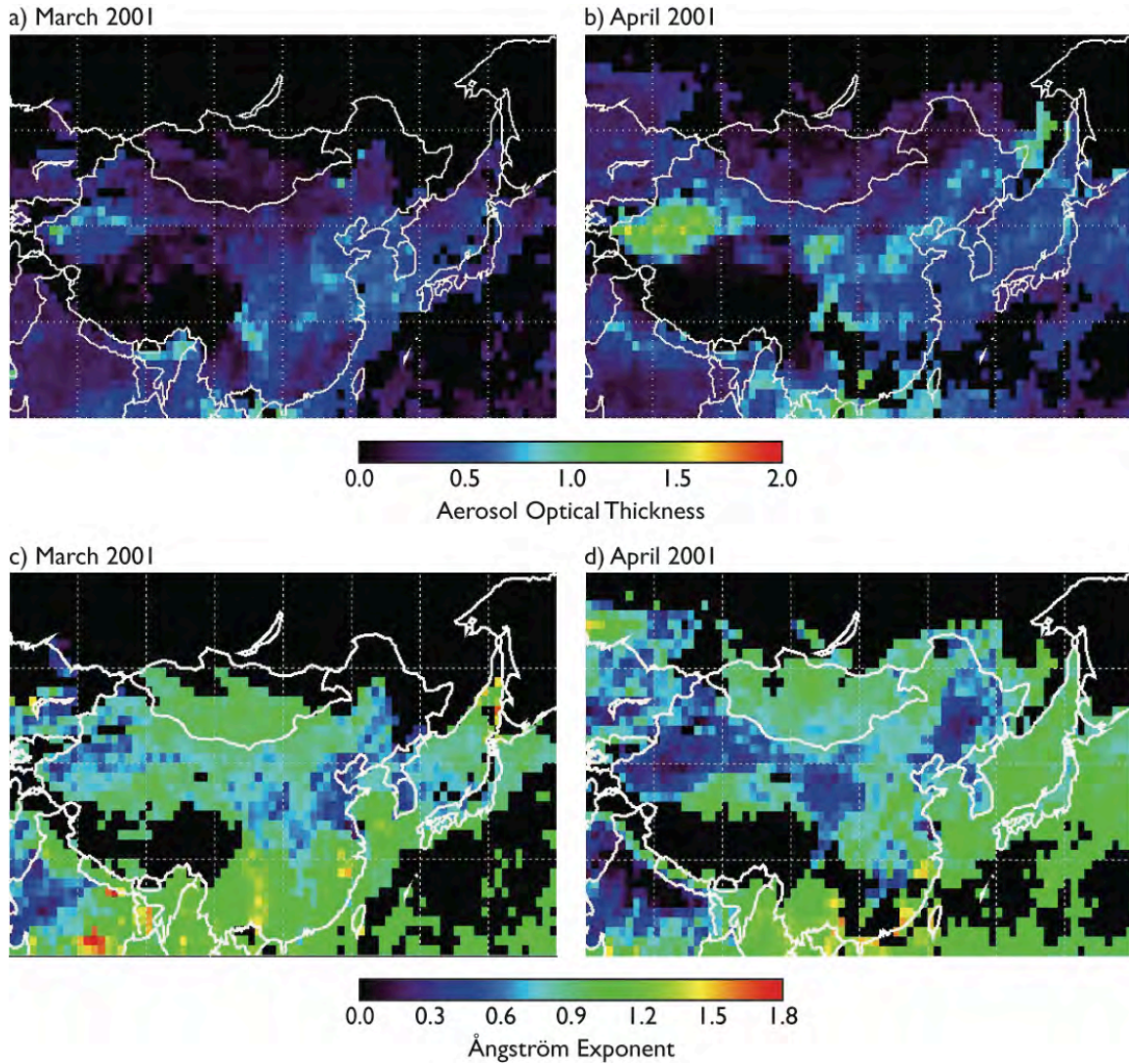
Figure 12. Monthly average of aerosol optical thickness at 500 nm and Ångström exponent (412-490 nm) retrieved from the SeaWiFS Deep Blue algorithm for each $1^{\circ} \times 1^{\circ}$ grid box in East Asia for March and April 2001. The black color represents the region where there are not enough samples for calculation of the monthly mean due to the presence of clouds or seasonal snow/ice cover.
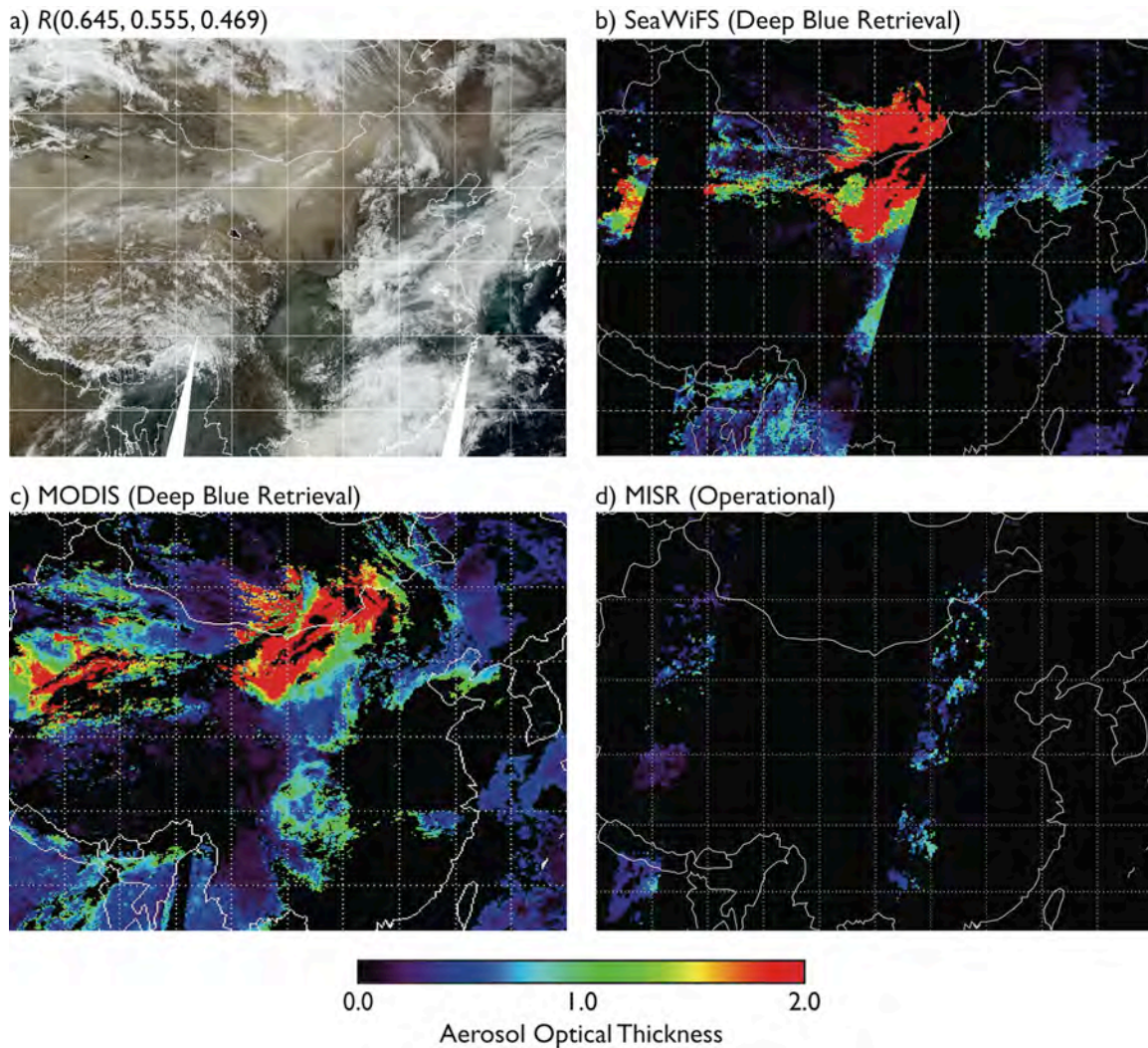
Figure 13. (a) Terra/MODIS true color image taken on April 6, 2001 reveals several dust storms over Mongolia and northwestern China. The corresponding daily level 2 maps of aerosol optical thickness retrieved from Deep Blue algorithm at mid-visible wavelength (i.e., 550 nm) are shown using (b) SeaWiFS and (c) MODIS reflectance measurements. The aerosol optical thickness from operational MISR products on the same day is also depicted in (d).

a) R(0.645, 0.555, 0.469)

b) SeaWiFS (Deep Blue Retrieval)

c) MODIS (Deep Blue Retrieval)

d) MISR (Operational)
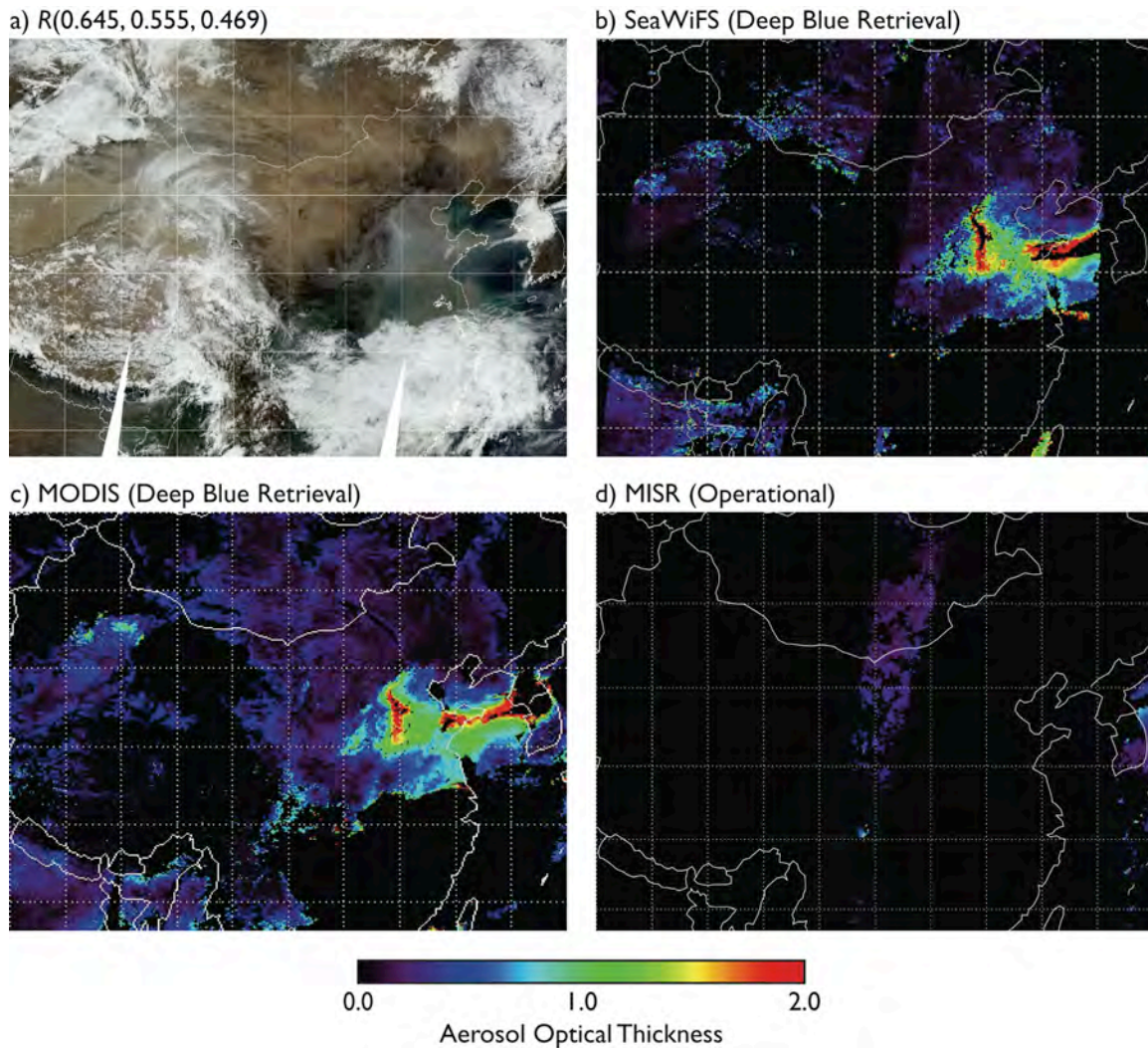

Aerosol Optical Thickness

Figure 14.   The extent of a severe pollution event over eastern China on April 2, 2001 is captured by (a) Terra/MODIS true color image. (b) and (c) display the corresponding level 2 distributions of aerosol optical thickness retrieved from Deep Blue algorithm at mid-visible wavelength (i.e., 550 nm) using SeaWiFS and MODIS measurements taken from this day, respectively. (d) Image of the aerosol optical thickness values derived from the operational algorithm for April 2 from MISR, which is also aboard on Terra, is shown over the same region.
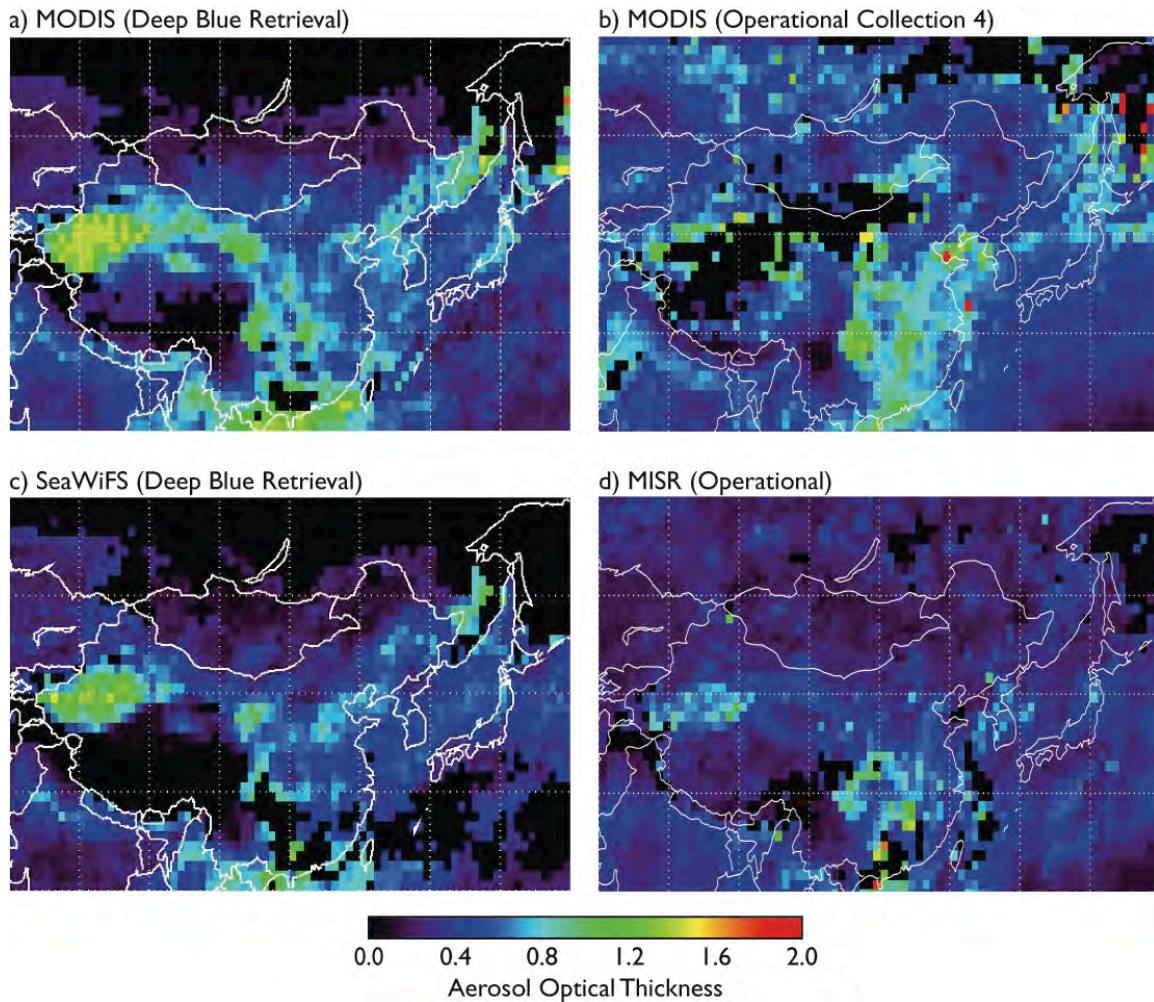
Figure 15. Monthly average aerosol optical thickness retrieved at mid-visible wavelength (i.e., 550 nm) from (a) the MODIS Deep Blue algorithm, (b) the MODIS collection 4 operational product, (c) the SeaWiFS Deep Blue algorithm, and (d) the MISR aerosol product for each $1^o \times 1^o$ grid box in East Asia for April 2001. The black color represents data gaps due to the presence of clouds or seasonal snow/ice cover (e.g., Deep Blue MODIS and SeaWiFS as well as MISR) and/or due to the bright reflecting surfaces (e.g., operational MODIS). Both the MODIS and SeaWiFS Deep Blue monthly means use criteria that require a minimum sample number of six cloud-free days, while the ones from MISR and MODIS collection 4 do not adopt such criteria.